Metasomatism and deformation of block-in-matrix structures in Syros: The role of inheritance and fluid-rock interactions along the subduction interface

Thomas Gyomlai, Philippe Agard, Horst R. Marschall, Laurent Jolivet, Axel Gerdes

Metasomatism and deformation of block-in-matrix structures in Syros: the role of inheritance and fluid-rock interactions along the subduction interface

Thomas Gyomlai[a,*], Philippe Agard[a], Horst R. Marschall[b,c,d], Laurent Jolivet[a], Axel Gerdes[b,c]

[a] Sorbonne Université, CNRS-INSU, Institut des Sciences de la Terre de Paris, ISTeP UMR 7193, F-75005 Paris, France

[b] Institut für Geowissenschaften, Goethe Universität, Altenhöferallee 1, 60438 Frankfurt am Main, Germany

[c] FIERCE, Goethe Universität, 60438 Frankfurt am Main, Germany

[d] Department of Geology & Geophysics, Woods Hole Oceanographic Institution, Woods Hole, Massachusetts 02543, USA

*Corresponding author (email: thomas.gyomlai@sorbonne-universite.fr; postal address: ISTeP - 4, Place Jussieu 75252 PARIS Cedex 05, France)

Keywords

Syros Island; Cycladic Blueschist unit; Mélange; Block-in-matrix structure; Metasomatism; Subduction interface

Abstract

The behavior of fluids at the subduction plate interface and their chemical and rheological impacts remain poorly constrained. Based on detailed fieldwork, petrographic and geochemical analyses and thermobarometry, the present study documents an example of a block-in-matrix 'mélange' metasomatized along the subduction interface (Kampos-Lia mélange zone, Cycladic Blueschists, Syros island). We show that this particular mélange zone is a preserved fragment of discontinuous oceanic domain associated with the Pindos basin, which underwent dominant exhumation-related deformation with top to the east shearing. A large part of the 'mélange' structure is inherited from the initial intraoceanic setting and should not be considered as a tectonic 'mélange'. Through exhaustive, meter-scale mapping of the nature of blocks and matrix we show that metasomatism dominantly occurs at the contact between metavolcanic layers and serpentinite, with diffusion of Ca from the metavolcanics to the matrix and diffusion of Mg in the opposite direction. Most of the metavolcanic layers and blocks (mafic and carbonate) are only partly digested contrary to the ultramafic matrix which has been largely metasomatized and forms a tremolite-chlorite-talc schist, i.e. a 'hybrid' rock with intermediate chemical composition. Geochemical data demonstrate that metasomatic element mobilization (e.g. Li, B, U, LILE and REE) varies at the scale of the unit, suggesting a complex evolution of fluid composition at the kilometer scale. We suggest that the fluid which intruded the Kampos subunit was derived from the subducting slab and caused an enrichment in Li, B, U, LILE (Rb, K, Na, Ba, Eu), MREE and HREE. Mineralogical and P-T constraints indicate that the dominant part of metasomatism and rock hybridization occurred during exhumation, at ~1 GPa, well after peak burial and detachment from the slab (~2 GPa). Due to the absence of major tectonic mixing and the scarce

preservation of prograde and peak metasomatic reactions, this metasomatism may be representative of fore-arc hybridization processes at depths of ~35 km. Deeper hybridization processes as hypothesized to produce a potential source for arc magmas are not well preserved in the studied examples. However, by changing the mineralogy of the matrix, metasomatism changes the rheological properties of the mélange and could thus manipulate the rheology of the subduction interface and influence exhumation processes.

1 Introduction

The interface between the downgoing slab and the mantle wedge exerts a fundamental control on element recycling, arc volcanism and seismicity in subduction zones (e.g., Stern 2002; Audet et al. 2009; Wada and Wang 2009; Marschall and Schumacher 2012; Spandler and Pirard 2013). However, chemical (Bebout, 2007) and physical processes (Agard et al., 2009, 2018) operating along the interface, and even its exact nature (i.e., lithologies, thickness, strain patterns, ...) remain ill-constrained. In particular, the net rheological and chemical impact of fluids at the subduction interface constitutes a major unknown which can only be addressed, at the m- to km-scale, by studying the fossil subduction rock record (Angiboust et al., 2015; Bebout and Penniston-Dorland, 2016).

Around the world, exhumed high pressure low temperature (HP-LT) units appear as either continuous slices or block-in-matrix structures, and have been used as a proxy to describe the plate interface (Guillot et al., 2015; Agard et al., 2018). Block-in-matrix structures are broadly coined in the literature as ’mélange’ zones (Hsü, 1968; Raymond, 1984; Grigull et al., 2012;

60 Bebout and Penniston-Dorland, 2016; Festa et al., 2019). Those mélange terranes have a wide
61 range in size (m- to km-scale), structure (block to matrix ratio, deformation features...), variety
62 of lithologies (e.g. pelitic, ultramafic or gneissic matrix), metamorphic grades (between 0.1 and 3
63 GPa and 150 to 800°C) and degree of metasomatism. Significant metasomatism is frequently
64 described and interpreted to progressively homogenize the various protoliths, forming 'hybrid'
65 rocks (Spandler et al., 2008; Marschall and Schumacher, 2012; Angiboust et al., 2014; Penniston-
66 Dorland et al., 2014; Bebout and Penniston-Dorland, 2016). Low-density hybrid rocks could form
67 'diapir' structures from the slab interface into the mantle wedge and directly contribute to arc
68 volcanism (Marschall and Schumacher, 2012; Nielsen and Marschall, 2017; Bayet et al., 2018;
69 Codillo et al., 2018).

70 The formation of block-in-matrix structures and metasomatism can occur before burial (e.g.,
71 hydrothermal circulation at the ridge, sedimentary mixing, discontinuity of the oceanic
72 lithosphere, core complexes formation), during the prograde or retrograde path (e.g.,
73 metasomatism through slab derived fluids, deformation and tectonic mixing) and after
74 exhumation (e.g., weathering, erosion). The behavior of the resulting block-in-matrix structure
75 (Stöckhert, 2002; Grigull et al., 2012) and the metasomatized rock rheology (Penniston-Dorland
76 et al., 2018) may have significant implications on the mechanical properties of the slab interface.
77 However, the significance and scale at which these processes occur, both in time and space, are
78 still mostly unconstrained.

79 Syros island (Fig. 1), in the Cycladic Archipelago, is renowned for its well-preserved eclogites
80 and blueschists and allows studying the tectonometamorphic evolution of a subduction
81 interface. In contact with metasediment-dominated units, km-scale mélange zones comprise

meta-igneous or metasedimentary lenses and blocks within an ultramafic serpentinite and/or chlorite-schist matrix (already described by Dixon, 1968). This ophiolitic unit is thought to belong to a restricted oceanic domain in the Pindos 'ocean' (Bonneau, 1984; Cooperdock et al., 2018; Schmid et al., 2020). Reaction zones at the contact between those different lithologies have been described for decades (Ktenas, 1907; Dixon, 1968; Ridley, 1984; Okrusch and Bröcker, 1990; Seck et al., 1996; Bröcker and Enders, 2001; Marschall et al., 2006). In particular, several studies have been performed on a m-scale continuous reaction zone (called the Lia beach transect in this study; Breeding et al. 2004; Miller et al. 2009; Pogge von Strandmann et al. 2015; Gorman et al. 2019). However, an understanding of the metasomatism at the scale of the mélange unit is still missing (Ague, 2007).

This study therefore aims to provide an image of a reacted plate interface 'mélange', through the example of Syros island, by studying both chemical and mechanical processes on a km-scale, trying to answer the following questions:

(1) What is the detailed organization (distribution, size and deformation of blocks and layers inside the matrix) of such a mélange, block-in-matrix structure? How does it relate to the original structure?

(2) Under which depth/temperature/deformation conditions did this metasomatism occur ? When did it happen in the overall subduction history ?

(3) What is the nature of the reaction zones and to what extent/scale do they depend on initial lithology, block size and/or matrix type? At the μm to m scale, what are the detailed transformations affecting rocks, minerals, and major and trace elements?

(4) Does the observed metasomatism produce chemically hybrid rocks, and to what extent ? What are the consequences of this mélange on the subduction interface rheology? Is this a relevant example to estimate arc magma sources ?

To approach these aims, we herein present a combined tectonometamorphic and geochemical approach (rock and mineral major and trace element compositions) with detailed field mapping between Kampos and Lia beach on the northern tip of the island, together with complementary investigations in Kini and Galissas (Fig. 1).

2 Geological setting

2.1 The Aegean domain

The Aegean domain corresponds to a collapsed segment of the Hellenic belt formed from the Late Cretaceous to the Early Eocene following subduction and collision of Africa with Eurasia (Le Pichon and Angelier, 1981; Bonneau and Kienast, 1982; Jolivet et al., 1994; Ring et al., 2010). During convergence, subducted HP-LT metamorphic units of the Cycladic Blueschist Unit (CBU) were exhumed beneath a top-to-the east/northeast thrust at the top and a top-to-the south detachment at the base (Augier et al., 2015; Huet et al., 2009; Trotet et al., 2001). From 35 to 30 Ma, the acceleration of African slab retreat led to the collapse of the Hellenic belt in the back-arc domain (Le Pichon and Angelier, 1981; Lister et al., 1984; Jolivet et al., 2004, 2013) and the exhumation of HP-LT units was completed via large-scale detachments, forming metamorphic core complexes (Lister et al., 1984; Urai et al., 1990; Gautier et al., 1993; Jolivet and Patriat, 1999), in a low-pressure and high-temperature (LP-HT) environment.

123 It has been proposed that the Cycladic Blueschist Unit may represent subducted fragments
124 of the Pindos oceanic domain (Bonneau and Kienast, 1982; Bonneau, 1984), but the oceanic
125 nature of this domain is somewhat controversial. Apart from thin ophiolitic slices, the CBU is
126 mostly associated with continental crust (Keay and Lister, 2002; Zlatkin et al., 2018) and no
127 ophiolite is found in the Pindos unit, i.e. in the non-metamorphosed equivalent of the CBU in the
128 mainland (Schmid et al., 2020). In the ophiolitic slices, metagabbros and metaplagiogranites
129 formed across a restricted time period only (mostly 76 to 81 Ma; Broecker and Enders, 1999;
130 Tomaschek et al., 2003; Bröcker and Keasling, 2006; Bulle et al., 2010; Bröcker et al., 2014;
131 Cooperdock et al., 2018); isotopic and trace element compositions of serpentinites from Syros
132 hint to a hyper-extended margin or refertilized mid-ocean ridge setting. If oceanic at all, the
133 Pindos basin was probably narrow and characterized by extended and thinned continental crust,
134 mantle exhumation, and incipient oceanic crust formation.
135 The Cycladic Archipelago (Fig. 1) is located in the center of the Aegean domain and
136 corresponds to the deepest exhumed portions of the Hellenides-Taurides belt. The CBU reached
137 peak-pressure conditions at 53-42 Ma (Trotet et al., 2001; Tomaschek et al., 2003; Putlitz et al.,
138 2005; Lagos et al., 2007; Lister and Forster, 2016; Laurent et al., 2017; Uunk et al., 2018).
139 Eclogites and blueschists of the CBU are spectacularly preserved on some of the islands. Syros
140 island, in particular, is world-famous for being the type locality of glaucophane (Hausmann,
141 1845), and has been the focus of numerous studies in geology, petrology, geochronology and
142 structural geology.

2.2 Tectonic units on Syros island

Most of the surface of Syros exposes the CBU except to the southeast, where the Vari Unit crops out (Fig. 1; Keiter et al. 2011; Laurent et al. 2017). The Vari Unit lies above and is separated from the CBU by a large-scale detachment (Trotet et al., 2001; Keiter et al., 2004, 2011; Soukis and Stockli, 2013). It is made of a greenschist-facies mylonitic unit overlain by orthogneiss intruded by amphibolite-facies metabasites. No HP imprint was recognized (Soukis and Stockli, 2013; Laurent et al., 2016).

Laurent et al. (2016) subdivided the Syros CBU nappe stacks into three subunits, based on their predominant lithology and metamorphic facies, bounded by top-to-the-east shear zones, which are, from bottom to top:

1) Posidonia Subunit, composed of gneiss overlain by albitic micaschists with intercalated boudins of metabasites and thin marble layers. Most of this subunit is overprinted under greenschist-facies conditions and only a few blueschist- and eclogite-facies parageneses are observed within the core of metabasite boudins.

2) Chroussa Subunit, composed of alternating micaschists, thick marble layers and metabasites. In this subunit, both eclogites and blueschist- and greenschist-overprinted eclogites are observed.

3) Kampos Subunit, mainly composed of a mélange of metabasites in an ultramafic matrix with minor metasediments and marbles. Eclogite- and blueschist-facies parageneses are particularly well preserved and mostly escaped significant retrogression. The Kampos and Chroussa subunits are bounded by the Kastri zone. The northern part of the island is composed

of a subunit structurally above the Kampos subunit, interpreted as a klippe of Chroussa Subunit and bounded by the Lia shear zone (Laurent et al., 2016).

The estimated age of maximum burial lies between 42 to 53 Ma (Tomaschek et al., 2003; Putlitz et al., 2005; Lagos et al., 2007; Lister and Forster, 2016; Laurent et al., 2017; Kotowski et al., 2020), whereas the age of syn-kinematic retrogression under greenschist-facies conditions has been estimated from 25 to 21 Ma (Bröcker et al., 2013) and 43 to 20 Ma (Kotowski et al., 2020).

The Kampos, Chroussa and Posidonia subunits were stacked by thrusting (Laurent et al., 2016), probably during the prograde evolution and at the pressure peak with a top-to-the S/ SW sense of shear (Philippon et al., 2011) and associated large-scale open folds (Keiter et al., 2011). Thrusting accounts for the structurally upper position of the Kampos ophiolitic slice on top of metasedimentary-dominated subunits (Keiter et al., 2004, 2011). During retrograde evolution and exhumation, deformation is accommodated along the major contacts or distributed within the whole Posidonia Subunit with a top-to-the-east sense of shear (Trotet et al., 2001; Laurent et al., 2016).

Metamorphic peak conditions were estimated in the range 450-530°C and in excess of 1.3 GPa up to 2.3 GPa by various authors, depending on the rocks and methods used (Okrusch and Bröcker 1990; Trotet et al. 2001; Rosenbaum et al. 2002; Keiter et al. 2004; Schumacher et al. 2008; Philippon et al. 2013; Lister and Forster 2016; Laurent et al. 2018; Kotowski et al. 2020). Laurent et al. (2018) obtained similar peak metamorphic P-T conditions from all three CBU subunits using independent thermobarometric methods at 2.2 ±0.2 GPa and 530 ± 30°C. They proposed a two-step retrograde P-T path: (1) first, exhumation under HP-LT conditions from 2.2

GPa to 1.0 GPa for all units and (2) second, isobaric heating at 1.0-1.2 GPa and 500-570°C for the two lowermost subunits (Chroussa and Posidonia). This heating is not observed in the upper Kampos subunit where peak parageneses are better preserved and the exhumation occurred under HP-LT conditions.

This heating phase was also identified on Tinos and Andros islands (Parra et al., 2002; Huet et al., 2015) and dated between 37 and 30 Ma (Bröcker et al., 1993, 2004; Huet et al., 2015). It coincides with a change in subduction dynamics around 30 Ma, with an increase in the rate of slab retreat, inducing major back-arc extension and marking the transition between a cold syn-orogenic regime in the subduction zone to a warmer post-orogenic regime in the back-arc domain (Parra et al., 2002; Jolivet and Brun, 2010; Laurent et al., 2018).

2.3 Mélange zone and metasomatism

Around the world, mélanges have been described as formations containing either similar or distinct blocks scattered within a weaker matrix (e.g., Franciscan mélange, Catalina Schists, New Caledonia, Syros, see Bebout and Penniston-Dorland 2016 for a review). On Syros Island, the Kampos subunit is characterized by the presence of block-in-matrix structures consisting of metamorphosed lenses and blocks of metasedimentary and meta-igneous rocks within a serpentinite and talc-chlorite-tremolite schist matrix. Several of those mélange zones are observed around the villages of Kampos, Kini, Galissas and near Syros airport. The contacts between these different lithologies are characterized by reaction zones, also called blackwalls or rinds (Ridley, 1984; Okrusch and Bröcker, 1990; Seck et al., 1996; Bröcker and Enders, 2001). Marschall et al. (2006) showed, by modelling fluid compositions, that the high $\delta^{11}B$ of

207 tourmalines from reaction zones (from +18 to +28‰) can be explained by the interaction
208 between slab-derived fluids and the blocks in the exhumation channel. Marschall et al. (2009)
209 documented high Li concentrations (up to 88 μg/g) and highly elevated Li/Be ratios (up to 80) in
210 metasomatic rinds, suggesting specific fluid enrichment in Li. They proposed that B/Be ratios are
211 dominantly controlled by the presence or absence of tourmaline and Cl/Be ratio variations could
212 be linked to fluid inclusions.

213 A meter-scale reaction zone between a metavolcanic and serpentinite, hereafter mentioned
214 as the Lia beach transect, has been studied in detail. Firstly, Breeding et al. (2004) noted a
215 preferential leaching of Large Ion Lithophile Elements (LILE), U and Pb by fluids in this reaction
216 zone. Miller et al. (2009) described five different zones: (I) glaucophane + garnet + phengite +
217 epidote, (II) glaucophane + epidote + chlorite, (III) chlorite + epidote + omphacite ± albite (IV)
218 chlorite ± titanite ± rutile ± apatite and (V) serpentine + chromite. They suggested a diffusion of
219 elements (such as Mg and Ca) through the reaction zone, and advective leaching of LILE and
220 enrichment in B and LREE by the fluid. Pogge von Strandmann et al. (2015) documented an
221 important decrease of the Mg isotopic composition (by ~1‰) through the reaction zone and
222 proposed a duration of the metasomatism of 100 kyr based on diffusion modelling. Finally,
223 Gorman et al. (2019) noticed a strong fluid mobilization of Os, Ir, Ru and Pt in this transect with
224 no influence of mechanical mixing and a minor advective enrichment in Re and Pd.

225 Contrasting P-T conditions were estimated for the formation of those reaction zones during
226 exhumation: at 1.17-1.23 GPa, 500-550°C (Breeding et al., 2004), at 0.62-0.72 GPa, 400-430°C
227 (Marschall et al., 2006) and at 1.2 GPa, 430°C Miller et al. (2009). This spread of estimated

pressures and temperatures could indicate that metasomatism occurred over a significant period of time with punctually short pulses of fluid influx (Pogge von Strandmann et al., 2015).

3 Kampos-Lia mélange zone mapping

This study focused on the Kampos subunit between Lia beach on the west coast of Syros and Kampos, and along the coast in Kini and Galissas (Fig. 1). The Kampos-Lia mélange zone is delimited by the Kastri and Lia shear zones (Laurent et al., 2016): the Kastri shear zone is the basal contact with the Chroussa Subunit, while the Lia shear zones is the roof contact with a klippe of similar lithology to the Chroussa Subunit. Those contacts are identified in the field thanks to shearing structures and lithological changes from the metavolcanic and/or ultramafic matrix of the Kampos subunit, to marbles and/or metapelites.

3.1 Major lithologies

Six main lithologies were recognized in the field:

(1) Metavolcanics are mainly composed of variable amounts of glaucophane, omphacite, garnet, epidote and lawsonite pseudomorphs. They form layers several meters thick. Felsic layers or dikes composed of jadeite and quartz are also found. More thinly foliated horizons are interpreted as reflecting a larger tuffitic component.

(2) Metagabbros are made of coarse-grained omphacite and clinozoisite with minor glaucophane replacing omphacite. This lithology is encountered in close association or within metavolcanic layers.

(3) Marbles form a meter-scale discontinuous, boudinaged marble horizon observed under the northern contact of the mélange zone. It resembles the laminated to massive, medium- to coarse-grained light gray marble, with frequent impurities, of the Chroussa subunit (visible at the contact south of the Kampos-Lia mélange zone).

(4) Chlorite ± tremolite ± talc schists matrix associated with blocks. Those blocks are centimeter to decameter scale and are mostly metabasites, Fe-Ti or Mg-Al-rich, or intermediate in composition. Blocks are partly rounded and metasomatized. For clarity, we will call 'rind' the metasomatized part of the blocks.

(5) Serpentinites are partly non-foliated, but are isotropic and are blocks themselves with preserved peridotite micro-textures (pyroxene pseudomorphs and mesh-textured serpentine-magnetite intergrowths). These serpentinites trend into sheared/foliated serpentinite and into talc- and chlorite-rich serpentinites where they transition into the chlorite ± talc schist.

(6) Micaschists are present at the northern contact of the mélange zone, where they are particularly deformed and show spectacular garnet-rich, centimeter to decameter scale sheath folds with mica, quartz and variable amounts of glaucophane, epidote and lawsonite (pseudomorphs).

3.2 Overall structure and deformation features

Metavolcanic layers are folded along W-E striking axes and show intense boudinage on the kilometer scale. These layers usually show a 30 to 80° dip to the N/NE (Fig. 2a). Lineations dominantly show a W-E orientation with some top to east indications. Well-preserved lawsonite pseudomorphs are often observed in layers alongside contacts and near the coastline.

GPS locations were taken for each matrix outcrop and block, distinguishing those still in place and those potentially later displaced by gravity sliding and erosion. Size, orientation of the long axis were measured for each block and their lithologic group and mineralogical composition of the rinds were determined. The nature of the matrix has been estimated with a spatial resolution of ~1 meter (Fig. 2a). In total, 499 matrix spots have been identified, with 45.1% of serpentinite, 4.6% of serpentinite and talc, 0.4% of talc, 1.6% of chlorite and talc, 13.4% of chlorite and tremolite with major chlorite, 17.6% of chlorite and tremolite with major tremolite and 17.2% of tremolite. This indicates that approximately half of the matrix comprises hybrid rocks (products of mixing or modal metasomatism). The serpentinite is never observed at the contact with blocks or metavolcanics. Consistently, the further the metavolcanic the more the matrix is made of serpentinite (e.g., near the northern contact; Fig. 2a).

Altogether 328 blocks have been identified (Figs. 2bcd), comprising 49.7% of Fe-Ti blocks, 30.2% of Mg-Al blocks and 15.5% of blocks intermediate in composition, 4% of metavolcanic blocks and 0.6% of metasedimentary blocks. The majority of blocks are Fe-Ti or have a Fe-Ti component. Block sizes range from centimeter to decameter sizes, most ranging between 1-2 meters with a length/width ratio usually between 1 and 2 with an E/NE-W/SW elongation and orientation (Fig. 2e), consistent with an overall EW stretching. The amount of block smaller than a meter may be underestimated because of the difficulty of observing them in the field. Several intermediate and Fe-Ti blocks (n=25) show pillow-lavas like structures and are mostly located in the northern part of the zone, as for the Mg-Al blocks (Fig. 2a).

Using m- to hm-scale observations, complemented by panorama and satellite pictures for careful extrapolation, a structural map has been realized (Fig. 2e). Pervasive top-to-the-east

shear sense is observed in the unit (Fig. 3), whether at the mineral scale or kilometer scale. It is outlined by the boudinage of layers of metavolcanics and marbles. A good example is the sheath folds affecting garnet-rich layers (Fig. 2f) observable along the Lia shear zone near the coast.

Detailed mapping reveals that most blocks lie in the variably metasomatized matrix. Metavolcanics can be mapped continuously and wrap around the blocks and matrix located in the core of a broad anticline. Therefore, those blocks form a tectonic horizon structurally beneath the metavolcanic layers. As a result, simplified cross-sections can be proposed based on a simple, first-order lithostratigraphic succession (Fig. 4). Our structural map based on m-scale observations broadly confirms the previous hm-scale mapping of Keiter et al. (2011; Fig. 1). It differs on the presence of a level of metasedimentary rocks described by Keiter et al. (2011), that we consider as a metavolcanic tuffitic component with a thinner foliation spacing and a greater abundance of phyllosilicates.

Our maps make it possible to estimate the proportion of the different lithologies in the Kampos-Lia mélange zone: 30.4% of matrix and blocks, 54.4% of metavolcanics, 1.0% of marble and 14.5% of quaternary ground cover. The cumulative area of the blocks corresponds to 2677 m^2, i.e. 2.5% of the matrix.

3.3 Block and matrix diversity

Samples were collected across different reaction zones to ensure representativeness (Table 1; Fig. 1). Mineral abbreviations are after Whitney and Evans (2010) except for tremolite (Trem). Two transects have been more thoroughly sampled:

(1) Transect L (Fig. 5), sampled near Lia beach, comprises 8 samples: n290, n57, n10 and n1 in a metavolcanic layer and p5, p125, p135 and p165 in the matrix. Numbers refer to the distance to the block/matrix contact in centimeters: n (for negative) refers to the distance into the block and p (for positive) for the distance away from the block (into the matrix).

(2) Transect G, sampled near Galissas, contains 7 samples: n50, n30, n8, n8b and n2 in a Fe-Ti block and p1 and p30 for the matrix.

Three main meta-igneous or metavolcanoclastic lithologies interact with the ultramafic matrix: Fe-Ti blocks, Mg-Al blocks and layers of metavolcanics. The different types of rinds developing at the contact with the matrix are displayed in figures 6 and 7. These rinds, identified by the disappearance and/or appearance of phases, replace the eclogitic or blueschist paragenesis. This suggests that they are mostly near peak and/or retrograde but the possibility remains that they witnessed earlier transformations (e.g. during peak burial). As shown by figures 6 and 7, the nature of the rinds largely depends on the nature of the block/layer (i.e. which lithologies were juxtaposed).

— Variations in the composition of metavolcanics are reflected, for example, by the presence or absence of quartz veins and lawsonite pseudomorphs (Fig. 6a). A decametric, weathered chloritic rind is observed on a few metavolcanics blocks (Fig. 6b). However, in almost all cases, metavolcanics are characterized by a decimetric rind of Gln+Ep+Ph ± Cpx, ± Chl, ± Ab (Fig. 6c). Whenever present, omphacite shows W-E stretching (Fig. 6d). Lawsonite pseudomorphs are still visible in the rind in places (Fig. 6e). Given that metavolcanics predominate in the block/layer lithology, this is the most common type of rind in the mélange. Finally, the specific well-studied outcrop north of Lia beach shows a meter-scale rind with a

Cpx+Chl+Ep association and then dominantly chlorite (Fig. 6f; similar to the Lia beach transect; Miller et al. 2009). Figure 6f also shows that the reaction limits are oblique with respect to the foliation.

— The Fe-Ti blocks show particularly large variations in block and rind mineral assemblages (Figs. 6,7). Fe-Ti blocks always contain garnet and rutile associated with glaucophane and/or omphacite (Figs. 6gh). A less widespread type of rind shows the presence of decimetric clinopyroxene growing perpendicular to the contact (Fig. 6i). The presence of fresh garnet grains in some Fe-Ti block rinds (Fig. 6j) seems to indicate early metasomatism at peak conditions or during early retrogression. Such an early metasomatism, if any, has been either very local or poorly preserved.

— The Mg-Al blocks mostly comprise clinopyroxene and/or glaucophane (Fig. 6k). Their rinds, in addition to clinopyroxene and/or glaucophane, are generally composed of chlorite, epidote, phengite, tourmaline and with rare occurrences of decimetric clinopyroxene similar to the one observed in Fe-Ti rinds.

Blocks intermediate in composition (Fig. 6l) often show pillow-like structures or microlithic dyke cross-cutting blocks and display complex rinds with assemblages similar to those of the Fe-Ti blocks.

4 Analytical methods

4.1 Electron probe microanalysis (EPMA) and Scanning electron microscope (SEM) analysis

EPMA and SEM were carried out at CAMPARIS (UPMC-IPGP, Paris, France) using a CAMECA SX-100 and a CAMECA SX-FIVE microprobes and the data reducing method of Pouchou and Pichoir (1991). Analytical conditions were 15 kV accelerating voltage and 10 nA specimen current for spot analyses and 15 kV accelerating voltage and 10 nA specimen current with a dwell time of 50 ms and a step size between 3 and 5 μm. Fe_2O_3, $MnTiO_3$, diopside, Cr_2O_3, orthoclase, anorthite and albite were used as standards.

Representative mineral compositions are provided in Table 2. The X-ray and backscattered electron compositional maps were processed using the program XMAPTOOLS 2.2.1 (Lanari et al., 2014).

4.2 Bulk-rock analysis

Eighteen mafic samples were sent for bulk-rock chemical analyses to the SARM (Nancy). Sample preparation consisted of fusion with $LiBO_2$ and dissolution in HNO_3. Major elements (SiO_2, Al_2O_3, Fe_2O_3, MnO, MgO, CaO, Na_2O, K_2O, TiO_2 and P_2O_5 with a detection limit less than or equal to 0.1%) and Sc were analyzed by inductively coupled plasma-optical emission spectroscopy (ICP-OES iCap6500). Trace element concentrations were determined by inductively coupled plasma mass spectrometry (ICPMS iCapQ). Boron was measured after fusion of the sample with sodium carbonate and measurement by UV-visible spectrophotometry of boron-carmine complex 40 in

concentrated sulfuric acid either directly or after concentration and separation on resin (detection limit of 0.5 µg/g for Li and 2 µg/g for B). Finally, Li was measured after acid attack of the sample with HF-$HClO_4$ and measurement with flame atomic absorption spectrometer. Whole rock compositions are given in Table 3.

4.3 LA-ICP-MS analysis

Extensive in-situ mineral analyses were performed using a Thermo Scientific Element 2 sector field laser ablation-inductively coupled plasma-mass spectrometry (LA-ICP-MS) at the Frankfurt Isotope & Element Research Center (FIERCE) of Goethe Universität Frankfurt. This ICP-MS is coupled to a Resolution S-155 (Resonetics) 193 nm ArF Excimer laser equipped with a two-volume ablation cell (Laurin Technic, Australia). Samples were ablated in a helium atmosphere and mixed in the ablation funnel with argon and nitrogen to minimize oxide production. Analyses were carried out using an 8Hz laser pulse rate, 40- or 60-µm diameter round spots .

Data were acquired in five independent analytical sessions for a total of 1687 analyses (counting GSD-1G, NIST-SRM612, BCR-2G and BHVO-2G reference material analyses). Each analysis consists of 21s background acquisition followed by 26 or 23.5s of sample ablation. During data acquisition, the signals of trace elements were detected by peak jumping in pulse counting mode, analogue mode or Faraday mode depending of the amount of signal with a total of 20 mass scans. Prior to analysis, each spot was pre-ablated for 6s to remove surface contamination.

GSD-1G reference glass was used for external sensitivity calibration and mean concentrations of SiO_2 determined by EPMA were used as internal standards. Data reduction

was done using the LADR program (Norris A, 2018), with limits of detection calculated for each element in every analysis.

After treatment, the data show a strong dispersion. This may be due to some important drift of the noise measurement during a session (probably due to vacuum variations), sometimes presence of inclusion in the standards and/or simplistic internal calibration. We herein only consider data whose sum of cations does not vary by more than 5% compared to the microprobe data. Summarized data are provided in supplementary material.

5 Petrography

We describe below mineral occurrences in the various transects, from block or layer to matrix.

Transect L (Lia; Figs. 5,8a) is composed of a metavolcanic layer (block: L_n290, L_n57; rind: L_n10 and L_n1) and matrix samples (L_p5, L_p125, L_p135 and L_p165). From L_n290 to L_n1, glaucophane represents more than half of the mineral mode. Garnet and epidote disappear and albite, phengite and chlorite progressively appear. Garnet grains mainly have quartz, epidote and glaucophane inclusions and are replaced by phengite in L_n10 and L_n1. L_n290 has the particularity of being cross-cut by a quartz vein. Variable amounts of tremolite, chlorite and talc characterize samples L_p5 to L_p135, with complete absence of tremolite in L_p125. Mineral grains are generally oriented parallel to the contact in L_n10, L_n1, L_p125 and L_p135, whereas L_p5 is chaotically deformed. Chlorite in L_p135 forms large-scale crystals with lenticular shapes in a tremolite-dominated matrix. In contrast L_p165 is mostly made of serpentine with a few percent of chlorite and talc.

411 Transect G (Galissas; Fig. 8b) is composed of a Fe-Ti rich block (block: G_n50, G_n30; rind:
412 G_n8, G_n8b, G_n2) and matrix samples (G_p1 and G_p30). The amounts of omphacite and
413 epidote vary between G_n50 and G_n8, and omphacite is no longer present in G_n2. The
414 amount of chlorite varies greatly, from 13% in G_p1 to 90% in G_n2. Garnet is increasingly
415 altered from G_n50 to G_n8b and absent in G_n2. Two single rounded crystals of chloritoid are
416 observed in G_n50. Rutile occurs in G_n50 to G_n8b, and rimmed by titanite in G_n2. In samples
417 G_n50 to G_n8b clinopyroxene is present both as large centimetric altered porphyroblasts and
418 as micrometric prismatic crystals forming localized aggregates. Sample G_n8b is crosscut by a
419 chlorite-tremolite vein perpendicular to the vein walls, similar to the matrix assemblage. Sample
420 G_n2 contains >80% chlorite with rutile, titanite and apatite. Sample G_p1 contains tremolite
421 and chlorite, while G_p30 contain chlorite oriented parallel to the contact.

422 Transect K (18, Kini) is composed of a Fe-Ti rich block and one matrix sample (K_18c).
423 Samples K_18a to d contain chlorite, clinopyroxene and garnet, together with minor rutile and
424 apatite. Garnet is partly altered and replaced by chlorite and hosts clinopyroxene inclusions in
425 both K_18b and e. Sample K_18c matrix assemblage comprises tremolite porphyroblasts and
426 chlorite.

427 Transect 9 (Lia) is composed of a Mg-Al-rich block (9a,b,c and d). Samples 9a, b and c are
428 mostly comprised of clinopyroxene, chlorite and epidote with variable amounts of
429 microcrystalline glaucophane and phengite, and minor amounts of albite and apatite. Sample 9d
430 is composed of chlorite and microcrystalline glaucophane.

431 Transect 19 (Lia) is composed of a Fe-Ti rich block (19a,b and c). Samples 19a and b are
432 mainly composed of euhedral garnet and glaucophane with quartz fringes around garnet and

433 minor phengite, paragonite, rutile and titanite. Sample 19c is dominantly made of
434 microcrystalline glaucophane and minor chlorite.

435 Other samples were collected to cover the whole range of existing lithologies (Fig. 7) and/or
436 to generalize and strengthen our observations.

437 Sample 22 is a metavolcanic rind with elongated aggregates of clinopyroxene surrounded by
438 glaucophane and phengite, together with minor albite. Sample 24b is a metavolcanic rind mostly
439 composed of centimetric pseudomorph of lawsonite with epidote, albite, chlorite and tremolite
440 associated with a glaucophane-dominated matrix. Sample 17 is from a metamorphosed acidic
441 dyke or vein with >90% quartz and some paragonite, albite and chlorite.

442 Sample 582 is a Fe-Ti block with cogenetic garnet, glaucophane, omphacite and minor rutile.
443 Sample 4 is a Fe-Ti-rich block with alternating clinopyroxene- and glaucophane-rich layers,
444 seemingly cogenetic garnet, minor rutile and phengite. Sample 27 is a Fe-Ti-rich rind with
445 glaucophane, epidote, clinopyroxene, phengite and minor albite, chlorite, altered garnet, rutile
446 and titanite.

447 Sample 21 is a Mg-Al-rich rind mostly composed of clinopyroxene, with subordinate amounts
448 of glaucophane, epidote, phengite and some tourmaline phenocrysts with clinopyroxene
449 inclusions. Sample 23 is a matrix sample composed mostly of chlorite and tremolite with major
450 rutile and minor apatite and titanite. Sample 581 is a serpentinite block with pervasive
451 replacement of serpentine by chlorite and minor talc.

6 Bulk-rock geochemistry

The bulk chemistry including major (Fig. 8) and minor (Fig. 9) elements allow recognizing four zones on transects L and G:

(1) the block interior with little or no metasomatism (L transect: n290, n57; G transect: n50, n30, n8), marked by low concentrations of Cr, Ni and Co, relatively low Mg, low enrichment in LREE.

(2) an inner rind (L: n10, n1; G: n2) characterized by marked changes in major element contents, and in particular a depletion in Ca, with strong variation of the mobile elements.

(3) a metasomatized matrix (L: p5, p125, p135; G: p1, p30) with high concentrations of Mg, Cr, Ni, Co and an enrichment in Ca. Samples are depleted in REE (with also a negative Eu anomaly), some particularly in LREE (L_p135 and L_p1) and one in HREE (L_p125). The strong variation of trace element contents is reflected by the strong variation of mineral assemblages.

(4) the serpentinite matrix (L_p165) with very high Mg, Cr, Ni and Co and very little Ca. Values obtained for L_p165 are similar to those obtained by Cooperdock et al. (2018), i.e. with no LREE addition, overall depletion of REE concentrations and lack of major Eu anomaly.

Figure 9a shows that the composition of the Fe-Ti block of transect G is similar to N-MORB. In contrast, the metavolcanic samples of transect L are intermediate between MORB and sediments and show a large tuffitic and/or sedimentary component (Fig. 9a).

Figure 9b compares our two main transects with the Lia beach transect of Miller et al. (2009). In both transects L and G, the evolution from block to rind is characterized by a decrease of Ca associated with an increase of Mg. This trend compares with the overall trend of Miller et al. (2009), yet no increase in Ca content, as reported in zone 3 by Miller et al., (2009), is

474 observed in our transects. Their zone 4 is similar to G_n2 in transect G, with a rind dominated by
475 chlorite and associated with titanite and apatite, yet they do not observe a tremolite-rich
476 metasomatized matrix with high Ca content. Miller et al. (2009) inferred that the original block-
477 matrix contact lied between their zones 4 and 5 (serpentinite). Some of our hybrid samples
478 show a higher Ca content than others described in Santa Catalina Island or New Caledonia (King
479 et al., 2006; Spandler et al., 2008).

480 The minor and major compositions of the metasomatized matrix are compatible with a
481 serpentinite protolith with high concentration of Mg, Cr and Ni (Fig. 8), negative Eu anomaly
482 (Fig. 9c), low REE concentration and similar concentration of relatively immobile elements such
483 as Al, Zr, Ti, V and Y (Figs. 8, 9d-h). The sharp drop of those element concentrations at the rind-
484 matrix contact suggests that the initial contact was located at the contact between the rind and
485 the matrix. No linear correlation is observed, however, between these relatively immobile
486 elements (Figs. 9d-f).

487 Figure 9c shows that the block and rind samples of transect L have similar Eu anomalies
488 (close to 1), while the block and rind samples of transect G show contrasting Eu anomalies (~1.3
489 and 0.7-0.9, respectively). Figure 9g and h show important variations (up to hundred times
490 more) in the concentration in REE and mobile elements such as B, Li and some LILE (Cs, Rb, K,
491 Na, Pb, Ba, Sr and Eu).

492 Ratios of normalized element concentrations of metasomatized samples with respect to
493 protolith concentrations are shown in figure 10a for transect L. Inferring the mobility of
494 elements is not straightforward, especially when comparing lithologies with contrasting
495 chemistries, i.e. mafic rocks with a variable sedimentary component with (potentially

496 metasomatized) ultramafic rocks. All measured elements may show some mobility with
497 metasomatism. Since we are interested in relative differences between the various transects,
498 the strategy followed here is to use only one relatively immobile element for normalization to
499 compare element gain/loss across all the transects.

500 In order to assess the extent of relative 'immobility', ratios of element concentrations in the
501 unmetasomatized and metasomatized rock were estimated. Values close to one, in all studied
502 cases, were mostly obtained for Al and all element concentrations were therefore normalized to
503 Al_2O_3. Samples used to compare metasomatized and unmetasomatized rocks were collected
504 close to one another to limit the influence of variations in initial composition. The spread of
505 initial variations is estimated in figure 8 based on our samples and published data (Pogge von
506 Strandmann et al., 2015; Cooperdock et al., 2018). Another advantage of Al_2O_3 is that this major
507 element can be analyzed to high accuracy and precision and is evenly distributed as a
508 constituent of the rock-forming minerals, contrary to minor elements which can be affected by
509 the presence of one extra grain of zircon, rutile or monazite/xenotime.

510 In detail, the concentration in the metasomatized rock is multiplied by the ratio of the Al_2O_3
511 concentration in the unmetasomatized rock and the Al_2O_3 concentration in the metasomatized
512 rock. Comparing ratios on either side of the contact (Rb=n1/n57 for the block; Rm=p5/p165 for
513 the matrix; Fig. 10a) enables assessing which elements are exchanged between the block and
514 the matrix (i.e., Rb>1 and Rm<1 for elements lost from the metasomatized matrix and gained by
515 the rind; or vice-versa: Rb<1 and Rm>1) and which ones are added (Rb and Rm>1 for higher
516 content alongside the contact than in both protoliths) or removed during fluid infiltration (Rb
517 and Rm<1 for lower content alongside the contact than in both protoliths). For the sake of

518 comparison, matrix gains and losses from transect L are evaluated using two different matrix
519 ratios (Rm=p5/p165 or Rm=p125/p165; Figs. 10b,c), while block gains and losses are compared
520 between transects L and G (Rb=n1/n57 or Rb=n2/n50; Figs. 10d,e).

521 The elements most affected by exchange along the contact are Ca and Mg. We see an
522 exchange of LREE, some LILE (Cs, Pb, Sr) and marginally some other elements such as Co and Ni
523 (Fig. 10a). The rind and metasomatized matrix are enriched in Li, B, U, some LILE (Rb, K, Na, Ba,
524 Eu), MREE and HREE. External loss, i.e. to an infiltrating fluid, characterizes Ga, Ta, Zn, Mn, P,
525 and marginally Cr from both the rind and the metasomatized matrix. The ratio for the block in
526 transect G (Fig. 10e) shows that, in contrast to the metavolcanic transect L, the rind is enriched
527 in Cr, Ta and Mn and depleted in Li, B, U, most LILE (Cs, Rb, K, Na, Pb, Ba, Sr) and HREE.

528 # 7 Mineral chemistry

529 ## 7.1 Chlorite

530 Chlorite shows a marked increase of XMg (Mg/(Mg+Fe_tot)) from block to matrix (from 0.39 to
531 0.88; Fig. 11a), associated with a decrease in Al content in the matrix (2Al from 2.40 to 1.46).
532 This variation in Mg content is mainly explained by the Fe-Mg substitution in all samples, and
533 the Tschermak substitution in the chlorite of the matrix and that of some of the rinds (19c and
534 G_n2), where chlorite is commonly hypersilicic (Si pfu from 2.87 to 3.36). Chlorite XMg in blocks
535 and rinds varies as a function of whole-rock compositions: 0.42-0.62 for transect L, ∼0.9 for
536 metavolcanics (e.g., 24b), 0.39-0.80 for Fe-Ti blocks and 0.6-0.8 for Mg-Al blocks.

7.2 Amphibole

Amphibole shows a wide range of compositions with XMg from 0.40 to 0.93 and XNa (Na/(Na+Ca)) from 0.02 to 0.99 (Fig. 11b). Two groups can be differentiated: (1) Na-rich amphibole in blocks and rind (XNa from 0.78 to 0.99) with glaucophane and a few magnesioriebeckite compositions and (2) Ca-rich amphibole in the matrix (e.g., G_n8b vein or 24b; XNa= 0.02-0.35) with tremolite, actinolite and a few winchite compositions (Leake et al., 1997). Sample 24b shows two types of amphibole with winchite compositions and intermediate XNa values (0.52 and 0.67). This sample shows the entire range of amphibole compositions from Na-rich to Ca-rich (XNa from 0.05 to 0.95) with a high XMg (from 0.82 to 0.90). Ca-rich amphibole has a higher XMg (from 0.75 to 0.93) compared to Na-rich amphibole (from 0.38 to 0.78, or 0.90 for 24b). In the matrix, amphibole shows a zoning in XMg content (e.g., p135; Fig. 11b, inset), with XMg ~0.83 in the core to ~0.93 in the rim. The XMg of amphibole in blocks and rinds also depends on whole-rock compositions, and is very close to that of chlorite: from 0.42 to 0.70 (transect L) or 0.90 (24b) for metavolcanics; from 0.38 to 0.68 for Fe-Ti blocks and from 0.61 to 0.78 for Mg-Al blocks.

7.3 Clinopyroxene

The composition of clinopyroxene (Fig. 12a) shows a wide range of composition Jd_{09-60} Acm_{00-48} Q_{21-76} (Q=diopside + hedenbergite + clinoenstatite + clinoferrosilite) and XMg from 0.31 to 0.80.

In transect G, measurements in altered clinopyroxene blasts (Jd_{12-46} Acm_{12-43} Q_{27-76}; XMg from 0.32 to 0.66) and the small metasomatic crystals (Jd_{09-53} Acm_{15-48} Q_{21-63}; XMg from 0.31 to 0.68) have similar values. An increase in Ca and Mg content is observed from block (Jd_{20-53} Acm_{17-48} Q_{21-43}; XMg from 0.31 to 0.58) to rind (Jd_{09-49} Acm_{12-40} Q_{27-76}; XMg from 0.44 to 0.68).

The same Ca and Mg increase is seen in transect 9, from 9a (Jd_{30-44} Acm_{10-22} Q_{38-54}; XMg from 0.53 to 0.72) to 9c (Jd_{23-44} Acm_{06-16} Q_{44-69}; XMg from 0.65 to 0.80), but not in transect K (Jd_{23-60} Acm_{00-21} Q_{36-74}; XMg from 0.51 to 0.79; comprising 18a: Jd_{32-49} Acm_{01-19} Q_{38-56}; XMg from 0.51 to 0.77). Peak clinopyroxene shows a narrower range of values compared to metasomatic clinopyroxene (e.g. 4 et 582: Jd_{32-48} Acm_{06-23} Q_{40-52}; XMg from 0.48 to 0.66).

7.4 Garnet

Zoned garnet is observed in transects G, L, 19 and samples 27 and 4 (Figs. 12b,c), with spessartine and pyrope content decreasing and increasing, respectively, from core (Alm_{51} Prp_3 Sps_{18} Grs_{32}) to rim (Alm_{71} Prp_{13} Sps_0 Grs_{20}), and XMg increasing from core (XMg=0.04) to rim (XMg=0.20).

Transect K shows two garnet populations: (1) In samples K_18a and d, one with similar composition to other samples, from core (Alm_{49} Prp_5 Sps_{13} Grs_{31}; XMg=0.09) to rim (Alm_{64} Prp_{15} Sps_0 Grs_{24}; XMg=0.21); (2) In samples K_18b and e, a higher spessartine and grossular content from core (Alm_{35} Prp_3 Sps_{29} Grs_{39}; XMg=0.09) to rim (Alm_{60} Prp_{14} Sps_1 Grs_{26}; XMg=0.21).

The second population of garnet shows inclusions of metasomatic clinopyroxene and is therefore interpreted as metasomatic garnet.

7.5 White mica

Phengitic compositions are observed in transect 9, with an increase in Mg content from block (Tri_4 Prl_1 Ms_{50} Cel_{41} Pg_4; XMg=0.68 ,Si pfu=3.41) to rind (Tri_4 Prl_1 Ms_{47} Cel_{41} Pg_7; XMg=0.74, Si pfu=3.42). A somewhat different trend is observed in transect L from block (block: Tri_8 Prl_{14} Ms_{45} Cel_{28} Pg_4, XMg=0.74, Si pfu=3.42) to rind (rind: Tri_8 Prl_{12} Ms_{45} Cel_{32} Pg_4; XMg=0.66, Si pfu= 3.44). Sample 19a shows a distinct population of mica (Tri_3 Prl_4 Ms_{50} Cel_{36} Pg_8, XMg=0.57, Si pfu=3.38)

Other samples have a wide range of mica compositions with dominant muscovite component: #4 (Tri_3 Prl_0 Ms_{49} Cel_{42} Pg_6, XMg=0.62, Si pfu=3.41), #21 (Tri_5 Prl_1 Ms_{53} Cel_{31} Pg_9, XMg=0.69, Si pfu= 3.31), #22 (Tri_3 Prl_1 Ms_{51} Cel_{41} Pg_5, XMg=0.7, Si pfu=3.40), #27 (Tri_3 Prl_1 Ms_{49} Cel_{38} Pg_{10}, XMg=0.68, Si pfu=3.37) and #n50 (Tri_7 Prl_1 Ms_{59} Cel_{25} Pg_8, XMg=0.53, Si pfu= 3.25).

Paragonite is observed in both samples 17 (Tri_1 Prl_2 Ms_4 Cel_0 Pg_{93}, XMg=0.27, Si pfu=3.01) and 19a (Tri_2 Prl_3 Ms_4 Cel_0 Pg_{91}, XMg=0.26, Si pfu=3.02).

7.6 Epidote

The composition of epidote varies in each sample, but the range of compositions does not significantly change between the different samples for a given transect. The range of compositions is as follows: Transect L (from 0.55 to 0.76 Fe^{3+} p.f.u.), transect G (from 0.63 to 0.86 Fe^{3+} p.f.u.), transect K (from 0.41 to 0.88 Fe^{3+} p.f.u.), 19b (from 0.41 to 0.76 Fe^{3+} p.f.u.), 17

595 (from 0.39 to 0.93 Fe^{3+} p.f.u.), 21 (from 0.48 to 0.68 Fe^{3+} p.f.u.), 24b (from 0.08 to 0.62 Fe^{3+}
596 p.f.u.), 4 (from 0.54 to 0.69 Fe^{3+} p.f.u.) and 9b (from 0.64 to 0.82 Fe^{3+} p.f.u.).
597

598 ### 7.7 Talc

599 In transect L, the Mg content of talc decreases closer to the block contact, from L_p165 (XMg
600 from 0.94 to 0.96), L_p135 (XMg from 0.94 to 0.95)to p125 (XMg=0.4). Samples G_p30 (XMg
601 from 0.93 to 0.96) and 581 (XMg from 0.94 to 0.96) show a similar range of Mg content.

602 ### 7.8 Serpentine

603 The serpentine is chemically homogenous in both L_p165 (XMg from 0.81 to 0.84) and 581 (XMg
604 from 0.87 to 0.88) , with a slightly higher Mg content in 581.

605 ### 7.9 Others

606 Two rounded chloritoid blasts are observed in sample G_n50 in transect G, with oscillatory Mg
607 zoning ($(Fe_{1.47-1.61}\ Mg_{0.45-0.66}\ Mn_{0-0.02})\ Al_{3.84-3.91}\ Si_{2.01-2.08}\ O_{10}\ (OH)_4$).
608 Sample 21 contains Na-Mg rich dravitic tourmaline (from 0.88 to 0.94 Na p.f.u.; from 0.02 to
609 0.06 Ca p.f.u and XMg from 0.74 to 0.79).

610 # 8 Trace element in-situ geochemistry

611 ### 8.1 Chlorite

612 Chlorite shows fairly flat REE spectra, except for a few analyses likely contaminated by inclusions
613 (mostly in transect G; Figs. 13ab), and a marked decrease in REE content from block to matrix. In

transects L and G, chlorite has a higher Ba content near the contact. In comparison, Cs and Rb contents increase in the rind of transect L (n1) but decrease at the contact of transect G (n2 and p1). Opposite trends are observed for Pb and Sr contents, which decrease from block to matrix in transect L and increase in transect G. The Li content decreases from block to matrix in transects L, G and K, except near the contact in transect L where L_p5 is slightly enriched compared to L_n1 (Fig. 14a). The Li content of chlorite in transects L and K is overall higher than in transect G. The Li content of chlorite in the matrix, far away from the contact, is generally very low (<5µg/g). In all three transects (with the exception of a few values for L_p135 in transect L), chlorite composition shows an increase in Ni and Cr from block to matrix, with a strong contrast at the contact (Fig. 14b). The Co content increases from block to matrix in transect L and G but decreases in transect K (Fig. 14c).

8.2 Amphibole

Na-amphibole (Fig. 13c) shows a wide range of REE spectra, from flat to enriched in LREE, and no significant nor systematic Eu anomaly. On average, Na-amphibole has higher Cr, Ni and Co contents in blocks compared to rinds (Figs. 14bc).

Ca-amphibole shows an enrichment in HREE and a negative anomaly of Eu. In transect L, REE contents are lower near the contact. In transect G, tremolite (in vein sample G_n8b) has a lower REE content compared to G_p1, and a less pronounced Eu anomaly. The range of Li, Co and LILE contents is similar in all samples (Fig. 14). In transect L, L_p5 and L_p135 have a similar Ni content, but L_p5 has a higher Cr content. Ca-amphibole in G_n8b is depleted in Cr, Ni, Th, Nb, Sc and enriched in Zr compared to G_p1. Ca-amphibole in transect K has a lower Ni and Co content on average than other transects.

8.3 Clinopyroxene

Clinopyroxene shows a trace element composition with HREE enrichment and a negative Eu anomaly in G_n8. Omphacite present in G_n8b (crosscut by a tremolite-chlorite vein) is enriched in REE, Sc, V and depleted in Ba, Ta, Zr, Hf compared to G_n8. The contents of Li, Cr, Co and Ni are similar in G_n8 and G_n8b with the exception of a few lower values of Cr in G_n8 (Fig. 14). Clinopyroxene in transect K (Fig. 14) shows similar Li, Cr and Ni contents as in transect G.

8.4 Garnet

Garnet shows classical HREE enrichment (Fig. 13g). Transects L and K show more dispersion of the data and higher values for LREE, Th, Nb and LILE than transect G. Garnet in transect K has lower Li and Cr contents and shows a marked Eu positive anomaly in the core (up to 11, Fig. 13h). The different trace element compositions of garnet in transect K further support the existence of a distinct generation of metasomatic garnet.

9 Thermobarometry

In order to determine the equilibrium conditions for the unmetasomatized metavolcanic rock of transect L (sample L_n57), thermodynamic modelling was performed in the NCKFMASHTO system using the Perple_X software (version 6.7.5, December 2016; Connolly 1990, 2005; see supplementary data). The thermodynamic dataset from Holland and Powell (1998) was used with the following set of activity models for solid solutions: garnet, epidote (Holland and Powell,

1998), chlorite (Holland et al., 1998), omphacite (Green et al., 2007), amphibole (Diener et al., 2007), feldspar (Holland and Powell, 2003), phengite (White et al., 2014) and talc as an ideal solution. Pseudosection calculation was performed with excess water, as justified by the abundance of hydrated phases. In the absence of carbonates in the studied sample, CO2 was neglected and a fixed water activity of 1 was used for the fluid. P-T conditions, estimated based on the Mg content of glaucophane and garnet and on the Fe^{3+} content of epidote, are around 530-550°C and 1.8-2 GPa. This value is similar to those estimated by most studies (Okrusch and Bröcker 1990; Trotet et al. 2001; Rosenbaum et al. 2002; Keiter et al. 2004; Schumacher et al. 2008; Philippon et al. 2013; Lister and Forster 2016; Laurent et al. 2018), indicating that the peak paragenesis of the block core in transect L is largely preserved.

In contrast, the nature of metasomatic minerals replacing the peak paragenesis suggests that most if not all of the rind formation process occurred during exhumation. For example, in transect L, garnet is replaced by phengite (Fig. 7b), which is the only K host. The addition of K, likely related to the metasomatic event, therefore occurred after garnet growth. In transect K, the composition of the garnet population in the rind differs from that in the block. Garnet from the rind also contains inclusions of metasomatic clinopyroxene, indicating formation after the inception of metasomatism (Fig. 7i).

In order to further assess the P-T conditions of metasomatism, thermobarometric calculations were performed for three samples (K_18e, 24b and L_p135) using Thermocalc V. 3.21 (Holland and Powell, 1998, 2011). The H_2O activity was set at 1.0 based on the lack of significant halogen

and carbon contents in hydrous minerals. Mineral activities were determined using the AX software (Holland and Powell, 1998; updated in 2011).

— Matrix sample L_p135 (L transect): the metasomatic assemblage of Ca-amphibole ($Na_{0.438}$ $Ca_{1.545}$ $Mg_{4.120}$ $Fe2+_{0.561}$ $Fe3+_{0.206}$ $Mn_{0.016}$ $K_{0.019}$ $Al_{0.285}$ $Si_{7.890}$ O_{22} $(OH)_2$), chlorite ($Mg_{4.153}$ $Fe2+_{0.838}$ $Mn_{0.009}$ $Al_{1.912}$ $Si_{3.063}$ O_{10} $(OH)_8$) and talc ($Mg_{2.794}$ $Fe2+_{0.138}$ $Si_{4.030}$ O_{10} $(OH)_2$) is unconstrained for pressure (1.90±1.99 GPa) but yield temperatures of 561±78°C.

— Rind sample 24b: the equilibrium assemblage made of Ca-amphibole ($Na_{0.507}$ $Ca_{1.538}$ $Mg_{3.905}$ $Fe2+_{0.565}$ $Mn_{0.015}$ $K_{0.029}$ $Al_{0.698}$ $Si_{7.870}$ O_{22} $(OH)_2$), chlorite ($Mg_{3.634}$ $Fe2+_{0.633}$ $Mn_{0.010}$ $Al_{2.214}$ $Si_{3.198}$ O_{10} $(OH)_8$) and albite ($Na_{0.964}$ $Al_{1.014}$ $Si_{2.995}$ O_8) is poorly constrained for temperature (505±155°C) but yield pressures around 1.02 ±0.15 GPa.

— Sample K_18e: using the garnet-clinopyroxene Fe-Mg exchange thermometer of Ravna (2000) at a pressure of 1.0 GPa, the garnet core ($Ca_{0.897}$ $Mn_{0.694}$ $Mg_{0.170}$ $Fe2+_{1.183}$ $Fe3+_{0.134}$ $Al_{1.977}$ $Si_{2.935}$ O_{12}) and clinopyroxene inclusion ($Ca_{0.494}$ $Na_{0.467}$ $Mg_{0.399}$ $Fe2+_{0.124}$ $Fe3+_{0.153}$ $Al_{0.379}$ $Si_{1.966}$ O_6) predicts a temperature of 561°C. We estimate an uncertainty of ±50° due to uncertainties in the AX software models. The assemblage of garnet rim ($Ca_{1.006}$ $Mn_{0.047}$ $Mg_{0.417}$ $Fe2+_{1.685}$ $Fe3+_{0.068}$ $Al_{1.999}$ $Si_{2.967}$ O_{12}), in direct contact with clinopyroxene ($Ca_{0.447}$ $Na_{0.497}$ $Mg_{0.399}$ $Fe2+_{0.112}$ $Fe3+_{0.088}$ $Al_{0.425}$ $Si_{1.992}$ O_6), chlorite ($Mg_{3.330}$ $Fe2+_{1.276}$ $Mn_{0.027}$ $Al_{2.487}$ $Si_{2.818}$ O_{10} $(OH)_8$), epidote ($Ca_{2.026}$ $Mn_{0.014}$ $Fe2+_{0.074}$ $Fe3+_{0.426}$ $Al_{2.565}$ $Si_{2.938}$ O_{12} (OH)) and albite ($Na_{1.001}$ $Al_{1.026}$ $Si_{2.978}$ O_8) yield pressures of 1.03 ±0.11 GPa for temperatures of 653±27°C.

Estimates for metasomatism therefore lie mostly between 0.90-1.15 GPa and 500-650°C. Around 1 GPa, the breakdown of serpentine should occur for temperatures above 600°C

(Wunder et al., 1997; Guillot et al., 2015). Serpentinite unaffected by metasomatism is still observed in significant amounts in the mélange unit (Fig. 2). Therefore, it is more likely that the Kampos-Lia mélange experienced a temperature between 500-600°C during metasomatism, and that the high temperature from the multi-mineral equilibrium in sample 18e is overestimated. Our results are consistent with the estimation made by Breeding et al. (2004) using Thermocalc (1.17-1.23 GPa and 500-550 °C). However, we find higher temperatures than estimated by Miller et al. (2009; 1.20 GPa and 430°C) using Perple_X (Connolly, 2005). Finally, the estimation of Marschall et al. (2006; 0.60-0.75 GPa and 400-430°C) for some tourmaline-chlorite-albite bearing reaction zones is both lower in temperature and pressure. It could represent a later stage of metasomatism during further exhumation.

10 Discussion

10.1 Mélange structure and deformation

The Kampos-Lia mélange zone, ascribed to the Pindos oceanic domain (Bonneau and Kienast, 1982; Bonneau, 1984), is mainly composed of metavolcanics (54.4% of the surface, Fig. 2) associated with an ultramafic matrix derived from or composed of serpentinite (34% of the surface). Blocks in the ultramafic matrix are mainly metagabbros, and some show meta-pillow like structure. Acidic or basaltic dikes are observed in the metavolcanics and in some blocks. Metavolcanics have a tuffitic and/or pelitic component (Fig. 9a). Marbles are mostly observed near the upper contact. The distribution of lithologies, with metavolcanic layers on top of serpentinite associated with gabbro (Figs. 2,3), and the abundance of serpentinites (variably

717 metasomatized) advocate for a slow-spreading oceanic realm dominated by mantle exhumation,
718 located close to the continental margin but further outboard than the Posidonia and Chroussa
719 units. Trace element compositions of Syros metabasites are consistent with an oceanic origin
720 (Marschall et al., 2009; Seck et al., 1996), with a stable isotope signature of seawater alteration
721 (Katzir et al., 2007; Putlitz et al., 2000; Seck et al., 1996).

722 Metavolcanic layers are folded with a west-east orientation and are structurally distinct from
723 the major part of the block-in-matrix structure (Figs. 2,4). This folding indicates north-south
724 shortening and is consistent with prograde thrusting deformation (Philippon et al., 2011; Keiter
725 et al., 2011; Laurent et al., 2016). Laurent et al. (2016) already proposed that the shear zones on
726 either side of the Kampos-Lia mélange zone (the Kastri and Lia shear zones) were prograde
727 thrusts later reactivated as top-to-the east shear zones during exhumation. At the scale of the
728 Kampos-Lia mélange zone, large-scale as well as outcrop-scale boudinage is indeed compatible
729 with top to the east shearing (Fig. 3). A boudinaged marble layer is observed near and parallel
730 to the north contact of the mélange zone. This shearing is observable all over Syros and
731 occurred during the syn- to post-blueschist facies exhumation (Laurent et al., 2016).

732 The overall organization and distribution of lithologies in the Kampos-Lia mélange is
733 therefore consistent with an oceanic or more likely an ocean-continent transitional domain.
734 These conclusions are consistent with the recent reappraisal of the Pindos oceanic domain as an
735 extended and thinned continental crust associated with mantle exhumation and incipient
736 oceanic crust formation during the Cretaceous (Cooperdock et al., 2018; Kotowski et al., 2020;
737 Schmid et al., 2020). Despite burial and exhumation-related deformation, an inherited internal
738 structure can still be recognized (Fig. 4), suggesting that tectonic disruption was far from being

739 complete. Unlike other mélange zones (e.g., Franciscan Complex, Catalina Schist or Northern
740 Serpentinite Mélange of Cuba), the Kampos-Lia mélange zone is not a chaotic mélange and
741 remained relatively coherent during burial and exhumation. A significant part of the 'mélange'
742 structure can therefore be ascribed to the initial oceanic structure rather than to deformation
743 along the plate interface.

744 This coherent structure and the absence of exotic blocks (with original lithology and/or
745 metamorphic grade) suggest a relatively low mechanical mixing, incompatible with the
746 incorporation of mantle wedge derived serpentinite. The geochemical study of Kampos sub-unit
747 serpentinites (Cooperdock et al., 2018) further support these conclusions. These authors
748 showed that the geochemical signature of Kampos serpentinites is consistent with derivation
749 from abyssal peridotites in a hyper-extended margin setting or mid-ocean ridge and fracture
750 zone environment (even if a certain overlap in trace elements patterns exists between the
751 different tectonic settings; Deschamps et al., 2013). While the occurrence of serpentinite mesh
752 texture has been associated with a late stage of serpentinization (Pogge von Strandmann et al.,
753 2015), the relatively low and heterogenous deformation in the mélange may have allowed for
754 the preservation of undeformed serpentinite. In conclusion, the Kampos-Lia block-in-matrix
755 structures essentially reflects lithological heterogeneities in an ocean-continent transitional
756 domain and did not undergo major mechanical mixing during burial and exhumation. The
757 Kampos Unit is therefore not a tectonic mélange as previously thought.

10.2 Blocks, rinds and matrix

The diversity of reaction zones seems to depend first and foremost on the nature of the protolith (Figs. 6,7). Whole-rock compositions, petrography and major/trace element mineral chemistry (Figs. 8-14) allows differentiating four parts in the reaction zones:

(1) blocks or layer, slightly metasomatized at most, retaining the eclogitic or blueschist-facies paragenesis dictated by the chemical nature of the protolith (e.g., Fe-Ti rich to Mg-Al rich).

(2) a rind, where the block/layer is thoroughly metasomatized. It generally comprises chlorite, amphibole, sodic pyroxene, albite, phengite, apatite and titanite. Large variations exist in whole-rock major (SiO_2, MgO, CaO) or incompatible elements (LILE, B, U, Li and some REE) and in mineral compositions.

(3) a metasomatized matrix chiefly composed of tremolite, chlorite and/or talc, with decreasing Ca and increasing Cr, Ni and Mg content, both in bulk chemistry and mineral composition, from the matrix/block contact to the serpentinite. Enrichment in incompatible elements (some REE, U and Li), particularly near the contact, is observed in the metasomatized matrix compared to the serpentinite.

(4) a serpentine matrix with various proportions of talc, with classic high Cr, Ni and Mg content and insignificant Ca.

The whole-rock concentrations of relatively immobile elements (Al, Zr, Ti, V, Y, Cr and Ni) and their sharp drop from rind to matrix (Figs. 8,9) suggest a serpentinite origin for the metasomatized matrix, and that the matrix/block 'front' did not move spatially during metasomatism. The main major elements exchanged across the contact are Mg (derived from

779 serpentinite) and Ca (derived from the blocks, Fig. 8). Metavolcanic layers, since they
780 predominate across the Kampos-Lia mélange at least, have the largest contribution to
781 metasomatic exchanges and transformation of matrix.

782 The two transects studied in detail (L,G; Fig. 15) show different trace element patterns.
783 Transect L (across metavolcanics) points to an enrichment in Li, U, LILE and HREE with a
784 significant exchange of B and LREE between the block and matrix (Fig. 15a). Transect G (across a
785 Fe-Ti-rich gabbro) points to an enrichment in LREE and depletion in U and LILE in the rind and
786 metasomatized matrix, and exchanges of HREE, Li and B between the block and matrix (Fig.
787 15b). These contrasts reveal the complexity of fluid-assisted exchanges in Kampos at subunit
788 scale.

789 The strong variation in Mg and Ca (Fig. 15) documented here is similar to that previously
790 observed in the Lia beach transect (Breeding et al., 2004; Miller et al., 2009). In this
791 metavolcanic rind, Breeding et al. (2004) observed a depletion in LILE and U without change in
792 REE concentration and Miller et al. (2009) observed a depletion in LILE but an enrichment in B
793 and LREE (Fig. 15c). The Lia beach transect, however, shows only very limited metasomatic
794 overprint of the serpentinite along the contact. The enrichment or depletion in LILE
795 concentration observed in this study has been documented in various metasomatized rocks, but
796 more particularly the enrichment for mafic and ultramafic rocks, which are initially poor in these
797 elements (Bebout, 2007; Bebout and Penniston-Dorland, 2016). Enrichment in LILE, usually
798 associated with phengite crystallization (such as in the rind of transect L), has been documented
799 for both prograde and retrograde metamorphism (e.g. in the Catalina Schist and Samana
800 Complex; Sorensen et al., 1997).

10.3 Fluid composition and behavior

Chemical exchanges during metasomatism can occur in several ways: (1) diffusion following a chemical potential gradient, (2) advection with fluid flow in fractures and intergranular spaces and (3) mechanical mixing.

Contrary to other mélanges (e.g., Catalina schist; Bebout and Barton, 2002; Bebout and Penniston-Dorland, 2016; Gorman et al. 2019), there is no evidence for mechanical mixing at the scale of a transect: clearly defined intermediate composition are not found (Figs. 8,9d-f) and element concentrations throughout the transects do not show systematic, diagnostic parallel evolutions (in the sense of Gorman et al. 2019, their figure 9b). In addition, no strong correlation is observed between relatively immobile elements (Figs. 9d-f). The rinds are moreover commonly foliated parallel to the inner block foliation, and do not show any additional deformation patterns which could be associated with incorporation and digestion of matrix clast(s). Nor do we observe any dismemberment of block or rind into the matrix. Mechanical mixing, if any, is therefore not a dominant process and is mostly hidden by advective and diffusive processes.

Element exchange is more likely controlled by advection at the scale of the unit (such as B, Li, U and LILE or Re and Pd; Gorman et al. 2019) with high enrichment or depletion along the contact. Other elements (such as Mg and Ca) are redistributed locally and strongly governed by local rock composition through diffusion in the intergranular fluid network at the meter scale, as demonstrated by Pogge von Strandmann et al. (2015). Pogge von Strandmann et al. (2015) estimated that the formation of the Lia Beach transect reaction zone may have taken ~100 ka, suggesting that the influx of fluids did not last throughout the entire exhumation process but

823 rather during one or several short events. A full integration of the entire reaction zone is
824 necessary to tell if REE were advectively moved in or out of the area and it remains to be
825 quantified how much of the REE are really mobilized over larger distances by fluid advection as
826 opposed to local redistribution across the growing contacts. Indeed, REE enrichment is generally
827 associated with the crystallization of accessory minerals such as epidote, apatite, monazite and
828 titanite (Miller et al., 2009; Sorensen and Grossman, 1993), which can form narrow domains in
829 the reaction zone. Relatively REE-enriched phases such as Ca-amphibole in the matrix (i.e.,
830 tremolite; Fig. 13) also participate in REE redistribution during fluid-rock interactions.
831
832 Significant fluid flow occurs where dynamic permeability is higher, namely at the contact
833 between sheared metavolcanics and the matrix, where Ca and Mg diffusion takes place. Fluid
834 flow is also expected in the high-permeability matrix, as suggested by numerical modeling
835 (Ague, 2007). In the matrix, tremolite is mainly present near blocks and layers but also as
836 patches with no visible associated block. Pathways and residence time of the fluid probably
837 dictate the location of tremolite pods in the metasomatized matrix and may explain differences
838 between transects across common metavolcanics (this study) and the Lia beach transect (Miller
839 et al., 2009).
840 Fluids have a dominant impact on the composition of rinds and metasomatized matrix in
841 mobile elements (e.g., Li, B, U, LILE and REE; Fig. 15). Differences between transects L, G and Lia
842 Beach suggest that fluid composition changes at the m- to hm-scale in the Kampos unit, and
843 through time, when migrating through the mélange zone and interacting with various
844 lithologies. If representative, transect L, which corresponds to the most common reaction zone

845 in the Kampos-Lia mélange, would indicate that infiltration of external fluid caused an
846 enrichment in Li, B, U, some LILE (Rb, K, Na, Ba, Eu), MREE and HREE (Figs. 9,10,15) and the fluid
847 was therefore probably enriched in these elements.

848 The rind of transect L shows very high Li concentrations (up to 45 μg/g). Marschall et al.
849 (2009) documented even higher Li concentrations in some metasomatized rocks of Syros (up to
850 88μg/g) and argued for an external fluid origin of Li. Based on high δ^{11}B values in tourmaline and
851 low silica activity (as a result of interaction with serpentinite), these authors argued for a slab-
852 derived fluid modified through migration along the subduction interface. This is also compatible
853 with the sulfur isotopic composition of metasomatic sulfides (Walters et al., 2019). Relatively
854 high fluid concentration in LILE along with Li, B and Pb has been attributed to interaction with
855 sedimentary rocks, given their enrichment in those elements compared to mafic and ultramafic
856 rocks (King et al., 2006; Penniston-Dorland et al., 2012). It is therefore likely that the
857 metasomatic fluid derived from the deeper dehydration in the downgoing slab was modified by
858 its infiltration into various lithologies (e.g. sedimentary and ultramafic) before reaching the
859 Kampos-Lia unit along the slab interface.

860 Finally, considering that metasomatism was probably rather short-lived ($\sim$100 ka integrated
861 duration; Pogge von Strandmann et al., 2015) and that fluid compositions vary largely at the
862 meter to hectometer scale, with some elements mobilized and advected over large distances or
863 redistributed locally and strongly governed by local rock composition, caution is needed when
864 extrapolating fluid composition to be representative of fluid-rock interactions at the scale of the
865 subduction plate interface.

10.4 Metasomatism in a subduction context?

10.4.1 Timing and significance of the CBU metasomatism in the subduction history

After entering subduction, the small CBU oceanic domain, typified by mantle exhumation and incipient oceanic crust formation, was sheared by top-to-the south reverse shear zones along the prograde path (Philippon et al., 2011; Laurent et al., 2016), and reached maximum burial between 42 and 53 Ma (Tomaschek et al., 2003; Putlitz et al., 2005; Lagos et al., 2007; Lister and Forster, 2016; Laurent et al., 2017). Tectonic slices of the CBU were then scrapped off the downgoing slab and underplated and/or started exhuming along the plate interface (Fig. 16b). Exhumation patterns are consistent with top-to-the east shearing (Trotet et al., 2001; Laurent et al., 2016).

Detachment from the slab may already have triggered the inflow of externally derived fluids and early metasomatism, at or near peak burial conditions, but supporting evidence is lacking for now. Instead, metasomatic minerals replacing the peak paragenesis suggest that most if not all of the rind formation process occurred during exhumation. Our estimates suggest that metasomatism occurred at 0.90-1.15 GPa and 500-600°C (Fig. 16a), hence much lower pressure than peak P-T conditions (530-550°C and 1.8-2 GPa; supplementary material). This is comparable with values documented by Laurent et al. (2018) for the Posidonia and Chroussa units, who related this slight isobaric heating to underplating at the base of the crust. Contrary to them, however, we suggest that some heating also affected the Kampos unit and that metasomatism began or largely developed at that time (Fig. 16c). This episode of heating could have played a role in the onset of significant fluid migration and metasomatism in the Kampos unit. It was

888 dated between 37 and 30 Ma on Tinos and Andros islands (Bröcker et al., 1993, 2004; Huet et
889 al., 2015). In support of this interpretation, Brooks et al. (2019) documented a fluid circulation
890 and entrapment during the late stages of exhumation on Sifnos beginning at about 1.0 GPa and
891 540°C. Those conditions were estimated using fluid inclusion microthermometry and are
892 consistent with this heating phase and our own PT estimations for the metasomatism in Syros.
893 Despite the m- to hm-scale block-in-matrix discontinuities/heterogeneities likely inherited
894 from the slow-spreading environment, data indicate that the Kampos-Lia mélange zone was only
895 mildly deformed and infiltrated by fluids during prograde and peak conditions or immediately
896 after the critical step of detachment from the slab (Agard et al., 2018) and incorporation along
897 the plate interface. Significant fluid ingression and metasomatism only occurred during
898 exhumation and heating. In this respect the Kampos-Lia mélange differs from a number of
899 studied mélanges interpreted as the result of prograde disaggregation and mechanical mixing
900 (e.g., the Santa Catalina schist, Penniston-Dorland et al. 2014, 2018), and/or retrograde mixing
901 of blocks with variable peak temperatures having witnessed fluid infiltration across a range of
902 metamorphic grades (e.g., Franciscan complex; Oh et al. 1991; Cooper et al. 2011; Wakabayashi
903 and Dilek 2011).

904 **10.4.2 Subduction interface metasomatism and rheology**

905 The data presented here show that exhumation-related metasomatism did not fully digest the
906 metavolcanic layers or competent blocks, at least not the largest ones. In contrast,
907 approximately half of the ultramafic matrix has been metasomatized (Fig. 2) and was
908 transformed into a hybrid rock with intermediate chemical composition, probably in part by

infiltrating subduction-derived fluids. Such hybridization could resemble the one inferred to occur deeper down in subduction zones, which may ultimately form hybrid buoyant diapirs feeding volcanic arcs (Marschall and Schumacher, 2012; Nielsen and Marschall, 2017; Codillo et al., 2018). The Syros example show, however, that no significant metasomatism and chemical mixing occurred in the slab during subduction, at least until peak conditions of ~2 GPa and 500-550°C were reached, despite the fact that it represents relatively deformable slow-spreading lithosphere (Ruh et al., 2015). This echoes the conclusions of Bayet et al. (2018), who suggested that metasedimentary diapirs may occur only at depth greater than 80 km and/or at some distance from the plate interface.

In the case of Syros, the low proportion of blocks in the matrix (2.5%) precludes any significant role of these blocks on the mechanical behavior of the Kampos unit as a whole, contrary to mélanges studied by Grigull et al. (2012; i.e., Ouaième Complex, New Caledonia; Rio San Juan Complex, Dominican Republic; Franciscan Complex and Santa Catalina schist, USA). It is likely that the hectometer to km-scale subcontinuous metavolcanic layers (Figs. 2-4), despite boudinage and mild digestion by metasomatism, had a much larger impact on the bulk rheology of the Kampos-Lia mélange zone.

The formation of both rheologically stiffer (tremolite) and weaker (chlorite and talc) matrix minerals at the expense of serpentinite may affect the rheology of the mélange in the context of exhumation along a plate contact. This is reminiscent of the Santa Catalina schist (Penniston-Dorland et al., 2018) where metasomatism induces the formation of hard minerals and may

929 increase the strength of the matrix. This may have to be considered to understand the
930 exhumation rheology along the subduction interface.

931 11 Conclusions

932 On Syros island, the presence of km-scale 'mélange' provides the opportunity to study
933 metasomatism and its impact along the subduction plate interface. The combination of detailed
934 mapping, structural, petrological and geochemical data suggests that:

935 (1) This mélange is, to a first approximation, composed of folded metavolcanics on top of an
936 ultramafic matrix hosting a limited block fraction (2-3vol%). This 'mélange' is a preserved
937 fragment of a discontinuous oceanic domain dominated by mantle exhumation, which was only
938 mildly tectonically disrupted during burial, and even exhumation. Deformation associated with
939 burial produced north-south folding whereas pervasive top-to-the-east boudinage prevailed
940 during exhumation, without significant tectonic mixing. This 'mélange' is not a tectonic mélange
941 as previously thought.

942 (2) Metasomatism occurred mostly, if not entirely, during exhumation, at ~0.90-1.15 GPa
943 and 500-600°C, probably in a context of underplating and isobaric heating.

944 (3) During metasomatism, Ca diffuses from blocks into the matrix (metasomatizing the
945 serpentinite) and Mg diffuses from the serpentinite into the blocks (forming a metasomatic rind
946 at the block margins). In detail, the variety of rinds largely depends on the block/layer lithology.
947 Significant mobilization of some elements (Li, B, U and LILE) by fluids is detected by whole-rock
948 and mineral compositions. Large variations nevertheless exist at the scale of the mélange,
949 suggesting a complex evolution of the fluid composition. Some elements are homogenized and

mobilized over larger scales (Li, B, U and LILE) and controlled by the advecting fluid, whereas other elements (Ca and Mg) are locally controlled by the rock compositions and only redistributed locally by diffusion across lithological boundaries.

(4) About half of the serpentinite matrix was metasomatized into a chlorite-tremolite-talc schist. This rock is chemically hybrid and most of it formed during exhumation. The Syros example also shows that no significant metasomatism and chemical mixing occurred within the slab, at least until the rocks reached peak conditions of ~2 GPa and 500-550°C, despite the fact that the Syros mélange represents relatively deformable slow-spreading partly oceanic lithosphere. Together with internal heterogeneities (i.e. metavolcanic layers), distributed metasomatism of the matrix (particularly tremolite formation) may have influenced the rheology and mechanical behavior of the mélange along the subduction interface during exhumation.

Acknowledgements

This study was partly funded by the project "Zooming in between plates" (Marie Curie International Training Network no. 604713) to P. Agard and by the ANR EGEO Project, from the European Research Council (ERC) under the seventh Framework Programme of the European Union (ERC Advanced Grant, grant agreement No 290864, RHEOLITH). We thank E. Delairis, O. Boudouma, M. Fialin and N. Rividi for technical and analytical support. Great thanks to many colleagues for insightful discussions, particularly A. Janin, M. Soret, C. Herviou, B. Lefeuvre, B. Dubacq and to E-FIRE scientists. We thank the reviewers of this manuscript B. Dragovic and S. Penniston-Dorland, as well as M. Scambelluri for his editorial handling.

References

Agard, P., Plunder, A., Angiboust, S., Bonnet, G., and Ruh, J., 2018. The subduction plate interface: Rock record and mechanical coupling (from long to short time scales). *Lithos*.

Agard, P., Yamato, P., Jolivet, L., and Burov, E., 2009. Exhumation of oceanic blueschists and eclogites in subduction zones: timing and mechanisms. *Earth-Science Reviews*, 92(12):53–79.

Ague, J. J., 2007. Models of permeability contrasts in subduction zone mélange: implications for gradients in fluid fluxes, Syros and Tinos Islands, Greece. *Chemical Geology*, 239(34):217–227.

Angiboust, S., Kirsch, J., Oncken, O., Glodny, J., Monié, P., and Rybacki, E., 2015. Probing the transition between seismically coupled and decoupled segments along an ancient subduction interface. *Geochemistry, Geophysics, Geosystems*, 16(6):1905–1922.

Angiboust, S., Pettke, T., De Hoog, J. C., Caron, B., and Oncken, O., 2014. Channelized fluid flow and eclogite-facies metasomatism along the subduction shear zone. *Journal of Petrology*, 55(5):883–916.

Audet, P., Bostock, M. G., Christensen, N. I., and Peacock, S. M., 2009. Seismic evidence for overpressured subducted oceanic crust and megathrust fault sealing. *Nature*, 457(7225):76– 78.

Augier, R., Jolivet, L., Gadenne, L., Lahfid, A., and Driussi, O., 2015. Exhumation kinematics of the Cycladic Blueschists unit and back-arc extension, insight from the Southern Cyclades (Sikinos and Folegandros Islands, Greece). *Tectonics*, 34(1):152–185.

990 Bayet, L., John, T., Agard, P., Gao, J., and Li, J.-L., 2018. Massive sediment accretion at 80 km
991 depth along the subduction interface: Evidence from the southern Chinese Tianshan. *Geology*,
992 46(6):495–498.

993 Bebout, G. E., 2007. Metamorphic chemical geodynamics of subduction zones. *Earth and*
994 *Planetary Science Letters*, 260(3-4):373–393.

995 Bebout, G. E. and Barton, M. D., 2002. Tectonic and metasomatic mixing in a highT, subduction-
996 zone mélange—insights into the geochemical evolution of the slab–mantle interface.
997 *Chemical Geology*, 187(1-2):79–106.

998 Bebout, G. E. and Penniston-Dorland, S. C., 2016. Fluid and mass transfer at subduction
999 interfaces—The field metamorphic record. *Lithos*, 240:228–258.

1000 Bonneau, M., 1984. Correlation of the Hellenide nappes in the south-east Aegean and their
1001 tectonic reconstruction. *Geological Society, London, Special Publications*, 17(1):517–527.

1002 Bonneau, M. and Kienast, J. R., 1982. Subduction, collision et schistes bleus; l'exemple de l'Egee
1003 (Grece). *Bulletin de la Société geologique de France*, 7(4):785–791.

1004 Breeding, C. M., Ague, J. J., and Broöcker, M., 2004. Fluid–metasedimentary rock interactions in
1005 subduction-zone mélange: implications for the chemical composition of arc magmas. *Geology*,
1006 32(12):1041–1044.

1007 Bröcker, M., Baldwin, S., and Arkudas, R., 2013. The geological significance of 40Ar/39Ar and Rb–
1008 Sr white mica ages from Syros and Sifnos, Greece: a record of continuous (re) crystallization
1009 during exhumation? *Journal of Metamorphic Geology*, 31(6):629–646.

1010 Bröcker, M., Bieling, D., Hacker, B., and Gans, P., 2004. High-Si phengite records the time of
1011 greenschist facies overprinting: implications for models suggesting mega-detachments in the
1012 Aegean Sea. *Journal of Metamorphic Geology*, 22(5):427–442.

1013 Bröcker, M. and Enders, M., 2001. Unusual bulk-rock compositions in eclogite-facies rocks from
1014 Syros and Tinos (Cyclades, Greece): implications for U–Pb zircon geochronology. *Chemical*
1015 *Geology*, 175(3-4):581–603.

1016 Bröcker, M. and Keasling, A., 2006. Ionprobe U-Pb zircon ages from the high-pressure/low-
1017 temperature mélange of Syros, Greece: age diversity and the importance of pre-Eocene
1018 subduction. *Journal of Metamorphic Geology*, 24(7):615–631.

1019 Bröcker, M., Kreuzer, H., Matthews, A., and Okrusch, M., 1993. 40Ar/39Ar and oxygen isotope
1020 studies of polymetamorphism from Tinos Island, Cycladic blueschist belt, Greece. *Journal of*
1021 *metamorphic Geology*, 11(2):223–240.

1022 Bröcker, M., Löwen, K., and Rodionov, N., 2014. Unraveling protolith ages of meta-gabbros from
1023 Samos and the Attic–Cycladic Crystalline Belt, Greece: Results of a U–Pb zircon and Sr–Nd
1024 whole rock study. *Lithos*, 198:234–248.

1025 Broecker, M. and Enders, M., 1999. U–Pb zircon geochronology of unusual eclogite-facies rocks
1026 from Syros and Tinos (Cyclades, Greece). *Geological Magazine*, 136(2):111–118.

1027 Brooks, H. L., Dragovic, B., Lamadrid, H. M., Caddick, M. J., & Bodnar, R. J., 2019. Fluid capture
1028 during exhumation of subducted lithologies: A fluid inclusion study from Sifnos, Greece.
1029 Lithos, 332, 120-134.

1030 Bulle, F., Bröcker, M., Gärtner, C., and Keasling, A., 2010. Geochemistry and geochronology of HP
1031 mélanges from Tinos and Andros, Cycladic blueschist belt, Greece. *Lithos*, 117(1-4):61–81.

1032 Codillo, E. A., Le Roux, V., and Marschall, H. R., 2018. Arc-like magmas generated by mélange-
1033 peridotite interaction in the mantle wedge. *Nature communications*, 9(1):2864.

1034 Connolly, J. A. D., 1990. Multivariable phase diagrams; an algorithm based on generalized
1035 thermodynamics. American Journal of Science, 290(6), 666-718.

1036 Connolly, J. A., 2005. Computation of phase equilibria by linear programming: a tool for
1037 geodynamic modeling and its application to subduction zone decarbonation. *Earth and*
1038 *Planetary Science Letters*, 236(1-2):524–541.

1039 Cooper, F. J., Platt, J. P., and Anczkiewicz, R., 2011. Constraints on early Franciscan subduction
1040 rates from 2-D thermal modeling. *Earth and Planetary Science Letters*, 312(12):69–79.

1041 Cooperdock, E. H., Raia, N. H., Barnes, J. D., Stockli, D. F., and Schwarzenbach, E. M., 2018.
1042 Tectonic origin of serpentinites on Syros, Greece: Geochemical signatures of abyssal origin
1043 preserved in a HP/LT subduction complex. *Lithos*, 296:352–364.

1044 Deschamps, F., Godard, M., Guillot, S., and Hattori, K., 2013. Geochemistry of subduction zone
1045 serpentinites: A review. *Lithos*, 178:96–127.

1046 Diener, J. F. A., Powell, R., White, R. W., & Holland, T. J. B., 2007. A new thermodynamic model
1047 for clino-and ortho-amphiboles in the system Na2O–CaO–FeO–MgO–Al2O3–SiO2–H2O–O.
1048 Journal of Metamorphic Geology, 25(6), 631-656.

1049 Dixon, J.E., 1968. The metamorphic rocks of Syros, Greece. Unveröff. Ph. D. Thesis Univ.
1050 Cambridge.

1051 Festa, A., Pini, G. A., Ogata, K., and Dilek, Y., 2019. Diagnostic features and field-criteria in
1052 recognition of tectonic, sedimentary and diapiric mélanges in orogenic belts and exhumed
1053 subduction-accretion complexes. *Gondwana Research*.

1054 Gautier, P., Brun, J.-P., and Jolivet, L., 1993. Structure and kinematics of upper Cenozoic extensional
1055 detachment on Naxos and Paros (Cyclades Islands, Greece). *Tectonics*, 12(5):1180–1194.

1056 Gorman, J., Penniston-Dorland, S., Marschall, H., and Walker, R., 2019. The roles of mechanical
1057 mixing and fluid transport in the formation of reaction zones in subduction related mélange:
1058 Evidence from highly siderophile elements. *Chemical Geology*, 525:96–111.

1059 Green, E., Holland, T., & Powell, R., 2007. An order-disorder model for omphacitic pyroxenes in
1060 the system jadeite-diopside-hedenbergite-acmite, with applications to eclogitic rocks.
1061 American Mineralogist, 92(7), 1181-1189.

1062 Grigull, S., Krohe, A., Moos, C., Wassmann, S., and Stöckhert, B., 2012. "Order from chaos": A
1063 field-based estimate on bulk rheology of tectonic mélanges formed in subduction zones.
1064 *Tectonophysics*, 568:86–101.

1065 Guillot, S., Schwartz, S., Reynard, B., Agard, P., and Prigent, C., 2015. Tectonic significance of
1066 serpentinites. *Tectonophysics*, 646:1–19.

1067 Hausmann JFL.,1845. Beiträge zur Oryktographie von Syra und ein neues Mineral, der
1068 Glaukophan. Göttinger Gelehrte Anzeigen 20: 193–198

1069 Holland, T., Baker, J., & Powell, R., 1998. Mixing properties and activity-composition
1070 relationships of chlorites in the system MgO-FeO-Al2O3-SiO2-H2O. European Journal of
1071 Mineralogy, 395-406.

1072 Holland, T. and Powell, R., 1998. An internally consistent thermodynamic data set for phases of
1073 petrological interest. *Journal of metamorphic Geology*, 16(3):309–343.

1074 Holland, T., & Powell, R., 2003. Activity–composition relations for phases in petrological
1075 calculations: an asymmetric multicomponent formulation. Contributions to Mineralogy and
1076 Petrology, 145(4), 492-501.

1077 Holland, T. J. B., & Powell, R., 2011. An improved and extended internally consistent
1078 thermodynamic dataset for phases of petrological interest, involving a new equation of state
1079 for solids. Journal of Metamorphic Geology, 29(3), 333-383.

1080 Hsü, K. J., 1968. Principles of melanges and their bearing on the Franciscan-Knoxville paradox.
1081 *Geological Society of America Bulletin*, 79(8):1063–1074.

1082 Huet, B., Labrousse, L., and Jolivet, L., 2009. Thrust or detachment? Exhumation processes in the
1083 Aegean: Insight from a field study on Ios (Cyclades, Greece). *Tectonics*, 28(3).

1084 Huet, B., Labrousse, L., Monié, P., Malvoisin, B., and Jolivet, L., 2015. Coupled phengite 40 Ar–39
1085 Ar geochronology and thermobarometry: PTt evolution of Andros Island (Cyclades, Greece).
1086 *Geological Magazine*, 152(4):711–727.

1087 Jolivet, L. and Brun, J.-P., 2010. Cenozoic geodynamic evolution of the Aegean. *International*
1088 *Journal of Earth Sciences*, 99(1):109–138.

1089 Jolivet, L., Daniel, J., Truffert, C., and Goffé, B., 1994. Exhumation of deep crustal metamorphic
1090 rocks and crustal extension in arc and back-arc regions. *Lithos*, 33(1-3):3–30.

1091 Jolivet, L., Faccenna, C., Huet, B., Labrousse, L., Le Pourhiet, L., Lacombe, O., Lecomte, E., Burov,
1092 E., Denèle, Y., Brun, J.-P., et al., 2013. Aegean tectonics: Strain localisation, slab tearing and
1093 trench retreat. *Tectonophysics*, 597:1–33.

1094 Jolivet, L. and Patriat, M., 1999. Ductile extension and the formation of the Aegean Sea.
1095 *Geological Society, London, Special Publications*, 156(1):427–456.

1096 Jolivet, L., Rimmelé, G., Oberhänsli, R., Goffé, B., and Candan, O., 2004. Correlation of syn-
1097 orogenic tectonic and metamorphic events in the Cyclades, the Lycian nappes and the
1098 Menderes massif. Geodynamic implications. *Bulletin de la Société Géologique de France*,
1099 175(3):217–238.

1100 Katzir, Y., Garfunkel, Z., Avigad, D., and Matthews, A., 2007. The geodynamic evolution of the
1101 Alpine orogen in the Cyclades (Aegean Sea, Greece): insights from diverse origins and modes
1102 of emplacement of ultramafic rocks. *Geological Society, London, Special Publications*,
1103 291(1):17–40.

1104 Keay, S. and Lister, G., 2002. African provenance for the metasediments and metaigneous rocks
1105 of the Cyclades, Aegean Sea, Greece. *Geology*, 30(3):235–238.

1106 Keiter, M., Ballhaus, C., and Tomaschek, F., 2011. *A new geological map of the Island of Syros*
1107 *(Aegean Sea, Greece): Implications for lithostratigraphy and structural history of the Cycladic*
1108 *Blueschist Unit*, volume 481. Geological Society of America.

1109 Keiter, M., Piepjohn, K., Ballhaus, C., Lagos, M., and Bode, M., 2004. Structural development of
1110 high-pressure metamorphic rocks on Syros island (Cyclades, Greece). *Journal of Structural*
1111 *Geology*, 26(8):1433–1445.

1112 Kelley, K. A., Plank, T., Ludden, J., and Staudigel, H., 2003. Composition of altered oceanic crust
1113 at ODP Sites 801 and 1149. *Geochemistry, Geophysics, Geosystems*, 4(6).

1114 King, R. L., Bebout, G. E., Moriguti, T., and Nakamura, E., 2006. Elemental mixing systematics and
1115 Sr–Nd isotope geochemistry of mélange formation: obstacles to identification of fluid sources
1116 to arc volcanics. *Earth and Planetary Science Letters*, 246(3-4):288–304.

1117 Kotowski, A. J., Behr, W. M., Cisneros, M., Stockli, D. F., Soukis, K., Barnes, J., & Ortega-Arroyo,
1118 D., 2020. Subduction, underplating, and return flow recorded in the Cycladic Blueschist Unit
1119 exposed on Syros Island, Greece. Earth and Space Science Open Archive ESSOAr.

1120 Ktenas, K.A., 1907. X. Die Einlagerungen im krystallinen Gebirge der Kykladen auf Syra und
1121 Sifnos. *Tschermaks mineralogische und petrographische Mitteilungen*, *26*(4), pp.257-320.

1122 Lagos, M., Scherer, E. E., Tomaschek, F., Münker, C., Keiter, M., Berndt, J., and Ballhaus, C., 2007.
1123 High precision Lu–Hf geochronology of Eocene eclogite-facies rocks from Syros, Cyclades,
1124 Greece. *Chemical Geology*, 243(1-2):16–35.

1125 Lanari, P., Vidal, O., De Andrade, V., Dubacq, B., Lewin, E., Grosch, E. G., and Schwartz, S., 2014.
1126 XMapTools: A MATLAB©-based program for electron microprobe X-ray image processing and
1127 geothermobarometry. *Computers & Geosciences*, 62:227–240.

Laurent, V., Huet, B., Labrousse, L., Jolivet, L., Monie, P., and Augier, R., 2017. Extraneous argon in high-pressure metamorphic rocks: Distribution, origin and transport in the Cycladic Blueschist Unit (Greece). *Lithos*, 272:315–335.

Laurent, V., Jolivet, L., Roche, V., Augier, R., Scaillet, S., and Cardello, G. L., 2016. Strain localization in a fossilized subduction channel: Insights from the Cycladic Blueschist Unit (Syros, Greece). *Tectonophysics*, 672:150–169.

Laurent, V., Lanari, P., Naïr, I., Augier, R., Lahfid, A., and Jolivet, L., 2018. Exhumation of eclogite and blueschist (Cyclades, Greece): Pressure–temperature evolution determined by thermobarometry and garnet equilibrium modelling. *Journal of Metamorphic Geology*, 36(6):769–798.

Le Pichon, X. and Angelier, J., 1981. The Aegean Sea. *Philosophical Transactions of the Royal Society of London. Series A, Mathematical and Physical Sciences*, 300(1454):357– 372.

Leake, B. E., Woolley, A. R., Arps, C. E., Birch, W. D., Gilbert, M. C., Grice, J. D., Hawthorne, F. C., Kato, A., Kisch, H. J., Krivovichev, V. G., et al., 1997. Nomenclature of amphiboles; report of the Subcommittee on Amphiboles of the International Mineralogical Association Commission on new minerals and mineral names. *Mineralogical magazine*, 61(405):295–310.

Lister, G. and Forster, M., 2016. White mica 40Ar/39Ar age spectra and the timing of multiple episodes of high-P metamorphic mineral growth in the Cycladic eclogite–blueschist belt, Syros, Aegean Sea, Greece. *Journal of Metamorphic Geology*, 34(5):401–421.

1147 Lister, G. S., Banga, G., and Feenstra, A. (1984). Metamorphic core complexes of Cordilleran type
1148 in the Cyclades, Aegean Sea, Greece. *Geology*, 12(4):221–225.

1149 Marschall, H. R., Altherr, R., Gméling, K., and Kasztovszky, Z., 2009. Lithium, boron and chlorine
1150 as tracers for metasomatism in high-pressure metamorphic rocks: a case study from Syros
1151 (Greece). *Mineralogy and Petrology*, 95(3-4):291.

1152 Marschall, H. R., Ludwig, T., Altherr, R., Kalt, A., and Tonarini, S., 2006. Syros metasomatic
1153 tourmaline: evidence for very high-δ11B fluids in subduction zones. *Journal of Petrology*,
1154 47(10):1915–1942.

1155 Marschall, H. R. and Schumacher, J. C., 2012. Arc magmas sourced from mélange diapirs in
1156 subduction zones. *Nature Geoscience*, 5(12):862.

1157 McDonough, W. F. and Sun, S.-S., 1995. The composition of the Earth. *Chemical geology*, 120(3-
1158 4):223–253.

1159 Miller, D. P., Marschall, H. R., and Schumacher, J. C., 2009. Metasomatic formation and
1160 petrology of blueschist-facies hybrid rocks from Syros (Greece): Implications for reactions at
1161 the slab–mantle interface. *Lithos*, 107(1-2):53–67.

1162 Nielsen, S. G. and Marschall, H. R., 2017. Geochemical evidence for mélange melting in global
1163 arcs. *Science Advances*, 3(4):e1602402.

1164 Norris A, D. L., 2018. Towards Estimating the Complete Uncertainty Budget of Quantified Results
1165 Measured by LA-ICP-MS. *Goldschmidt*.

1166 Oh, C. W., Liou, J., and Maruyama, S., 1991. Low-temperature eclogites and eclogitic schists in
1167 Mn-rich metabasites in Ward Creek, California; Mn and Fe effects on the transition between
1168 blueschist and eclogite. *Journal of Petrology*, 32(2):275–302.

1169 Okrusch, M. and Bröcker, M., 1990. Eclogites associated with high-grade blueschists in the
1170 Cyclades archipelago, Greece: a review. *European Journal of Mineralogy*, pages 451–478.

1171 Parra, T., Vidal, O., and Jolivet, L., 2002. Relation between the intensity of deformation and
1172 retrogression in blueschist metapelites of Tinos Island (Greece) evidenced by chlorite–mica
1173 local equilibria. *Lithos*, 63(1-2):41–66.

1174 Penniston-Dorland, S. C., Bebout, G. E., von Strandmann, P. A. P., Elliott, T., and Sorensen, S. S.,
1175 2012. Lithium and its isotopes as tracers of subduction zone fluids and metasomatic
1176 processes: Evidence from the Catalina Schist, California, USA. *Geochimica et Cosmochimica*
1177 *Acta*, 77:530–545.

1178 Penniston-Dorland, S. C., Gorman, J. K., Bebout, G. E., Piccoli, P. M., and Walker, R. J., 2014.
1179 Reaction rind formation in the Catalina Schist: Deciphering a history of mechanical mixing and
1180 metasomatic alteration. *Chemical Geology*, 384:47–61.

1181 Penniston-Dorland, S. C., Kohn, M. J., and Piccoli, P. M., 2018. A mélange of subduction
1182 temperatures: Evidence from Zr-in-rutile thermometry for strengthening of the subduction
1183 interface. *Earth and Planetary Science Letters*, 482:525–535.

1184 Philippon, M., Brun, J.-P., and Gueydan, F., 2011. Tectonics of the Syros blueschists (Cyclades,
1185 Greece): From subduction to Aegean extension. *Tectonics*, 30(4).

1186 Philippon, M., Gueydan, F., Pitra, P., and Brun, J.-P., 2013. Preservation of subduction related
1187 prograde deformation in lawsonite pseudomorph-bearing rocks. *Journal of Metamorphic*
1188 *Geology*, 31(5):571–583.

1189 Pogge von Strandmann, P. A., Dohmen, R., Marschall, H. R., Schumacher, J. C., and Elliott, T.,
1190 2015. Extreme magnesium isotope fractionation at outcrop scale records the mechanism and
1191 rate at which reaction fronts advance. *Journal of Petrology*, 56(1):33–58.

1192 Pouchou, J.L. and Pichoir, F., 1991. Quantitative analysis of homogeneous or stratified
1193 microvolumes applying the model "PAP". In Electron probe quantitation (pp. 31-75). Springer,
1194 Boston, MA.

1195 Putlitz, B., Cosca, M., and Schumacher, J., 2005. Prograde mica 40Ar/39Ar growth ages recorded
1196 in high pressure rocks (Syros, Cyclades, Greece). *Chemical Geology*, 214(1-2):79– 98.

1197 Putlitz, B., Matthews, A., and Valley, J. W., 2000. Oxygen and hydrogen isotope study of high-
1198 pressure metagabbros and metabasalts (Cyclades, Greece): implications for the subduction of
1199 oceanic crust. *Contributions to Mineralogy and Petrology*, 138(2):114–126.

1200 Ravna, K., 2000. The garnet–clinopyroxene Fe2+–Mg geothermometer: an updated calibration.
1201 *Journal of metamorphic Geology*, 18(2):211–219.

1202 Raymond, L. A., 1984. Classification of melanges. *Melanges: their nature, origin, and*
1203 *significance: Geological Society of America Special Paper*, 198:7–20.

1204 Ridley, J., 1984. Evidence of a temperature-dependent 'blueschist'to 'eclogite' transformation in
1205 high-pressure metamorphism of metabasic rocks. *Journal of Petrology*, 25(4):852–870.

1206 Ring, U., Glodny, J., Will, T., and Thomson, S., 2010. The Hellenic subduction system: high-
1207 pressure metamorphism, exhumation, normal faulting, and large-scale extension. *Annual*
1208 *Review of Earth and Planetary Sciences*, 38:45–76.

1209 Rosenbaum, G., Avigad, D., and Sánchez-Gómez, M., 2002. Coaxial flattening at deep levels of
1210 orogenic belts: evidence from blueschists and eclogites on Syros and Sifnos (Cyclades,
1211 Greece). *Journal of Structural Geology*, 24(9):1451–1462.

1212 Ruh, J. B., Le Pourhiet, L., Agard, P., Burov, E., and Gerya, T. (2015). Tectonic slicing of subducting
1213 oceanic crust along plate interfaces: Numerical modeling. *Geochemistry, Geophysics,*
1214 *Geosystems*, 16(10):3505–3531.

1215 Schmid, S. M., Fügenschuh, B., Kounov, A., Mațenco, L., Nievergelt, P., Oberhänsli, R., Pleuger, J.,
1216 Schefer, S., Schuster, R., Tomljenović, B., et al., 2020. Tectonic units of the Alpine collision
1217 zone between Eastern Alps and western Turkey. *Gondwana Research*, 78:308–374.

1218 Schumacher, J. C., Brady, J. B., Cheney, J. T., and Tonnsen, R. R., 2008. Glaucophane bearing
1219 marbles on syros, greece. *Journal of Petrology*, 49(9):1667–1686.

1220 Seck, H. A., Koetz, J., Okrusch, M., Seidel, E., and Stosch, H.-G., 1996. Geochemistry of a meta-
1221 ophiolite suite: an association of metagabbros, eclogites and glaucophanites on the island of
1222 Syros, Greece. *European Journal of Mineralogy*, pages 607–624.

1223 Sorensen, S. S. and Grossman, J. N., 1993. Accessory minerals and subduction zone
1224 metasomatism: a geochemical comparison of two mélanges (Washington and California,
1225 USA). *Chemical Geology*, 110(1-3):269–297.

1226 Sorensen, S. S., Grossman, J. N., and Perfit, M. R., 1997. Phengite-hosted LILE enrichment in
1227 eclogite and related rocks: implications for fluid-mediated mass transfer in subduction zones
1228 and arc magma genesis. *Journal of Petrology*, 38(1):3–34.

1229 Soukis, K. and Stockli, D. F., 2013. Structural and thermochronometric evidence for multistage
1230 exhumation of southern Syros, Cycladic islands, Greece. *Tectonophysics*, 595:148– 164.

1231 Spandler, C., Hermann, J., Faure, K., Mavrogenes, J. A., and Arculus, R. J., 2008. The importance
1232 of talc and chlorite "hybrid" rocks for volatile recycling through subduction zones; evidence
1233 from the high-pressure subduction mélange of New Caledonia. *Contributions to Mineralogy*
1234 *and Petrology*, 155(2):181–198.

1235 Spandler, C. and Pirard, C., 2013. Element recycling from subducting slabs to arc crust: A review.
1236 *Lithos*, 170:208–223.

1237 Stern, R. J., 2002. Subduction zones. *Reviews of geophysics*, 40(4):3–1.

1238 Stöckhert, B., 2002. Stress and deformation in subduction zones: insight from the record of
1239 exhumed metamorphic rocks. *Geological Society, London, Special Publications*, 200(1):255–
1240 274.

1241 Sun, S.-S. and McDonough, W. F., 1989. Chemical and isotopic systematics of oceanic basalts:
1242 implications for mantle composition and processes. *Geological Society, London, Special*
1243 *Publications*, 42(1):313–345.

1244 Tomaschek, F., Kennedy, A. K., Villa, I. M., Lagos, M., and Ballhaus, C., 2003. Zircons from Syros,
1245 Cyclades, Greece—recrystallization and mobilization of zircon during high-pressure
1246 metamorphism. *Journal of Petrology*, 44(11):1977–2002.

1247 Trotet, F., Vidal, O., and Jolivet, L., 2001. Exhumation of Syros and Sifnos metamorphic rocks
1248 (Cyclades, Greece). New constraints on the PT paths. *European Journal of Mineralogy*,
1249 13(5):901–902.

1250 Urai, J., Schuiling, R., and Jansen, J., 1990. Alpine deformation on naxos (Greece). *Geological*
1251 *Society, London, Special Publications*, 54(1):509–522.

1252 Uunk, B., Brouwer, F., ter Voorde, M., and Wijbrans, J., 2018. Understanding phengite argon
1253 closure using single grain fusion age distributions in the Cycladic Blueschist Unit on Syros,
1254 Greece. *Earth and Planetary Science Letters*, 484:192–203.

1255 Wada, I. and Wang, K., 2009. Common depth of slab-mantle decoupling: Reconciling diversity and
1256 uniformity of subduction zones. *Geochemistry, Geophysics, Geosystems*, 10(10).

1257 Wakabayashi, J. and Dilek, Y., 2011. Mélanges of the Franciscan Complex, California: Diverse
1258 structural settings, evidence for sedimentary mixing, and their connection to subduction
1259 processes. *Mélanges: processes of formation and societal significance: Geological Society of*
1260 *America Special Paper*, 480:117–141.

1261 Walters, J.B., Cruz-Uribe, A.M. and Marschall, H.R., 2019. Isotopic compositions of sulfides in
1262 exhumed high-pressure terranes: implications for sulfur cycling in subduction zones.
1263 Geochemistry, Geophysics, Geosystems, 20(7), pp.3347-3374.

1264 White, R. W., Powell, R. O. G. E. R., Holland, T. J. B., Johnson, T. E., & Green, E. C. R., 2014. New
1265 mineral activity–composition relations for thermodynamic calculations in metapelitic systems.
1266 Journal of Metamorphic Geology, 32(3), 261-286.

1267 Whitney, D. L. and Evans, B. W., 2010. Abbreviations for names of rock-forming minerals.
1268 *American mineralogist*, 95(1):185–187.

1269 Wunder, B. and Schreyer, W., 1997. Antigorite: High-pressure stability in the system MgO SiO2
1270 H2O (MSH). Lithos, 41(1-3), pp.213-227.

1271 Zlatkin, O., Avigad, D., and Gerdes, A., 2018. New detrital zircon geochronology from the cycladic
1272 basement (Greece): Implications for the paleozoic accretion of Peri-Gondwanan Terranes to
1273 Laurussia. *Tectonics*, 37(12):4679–4699.

1274

1275 **Tables**

1276

Transect	Samples	Location	Lithology	Mineralogy																			Lat. N/Lon. E
				Grt	Lws	Na-Amp	Ep	Cpx	Ph	Pg	Ab	Chl	Ca-Amp	Tlc	Srp	Rt	Ttn	Qz	Ap	Tur	Cld	Ox	
Transect L	n290	Lia	metavolcanic	x		x	x		x		x	x				x		x	x			x	37.4924/24.9087
	n57		metavolcanic	x		x	x		x		x	x				x	x					x	
	n10		rind	x		x	x		x		x	x				x	x					x	
	n1		rind			x	x		x		x	x				x	x		x			x	
	p5		matrix									x	x				x		x				
	p125		matrix									x		x								x	
	p135		matrix									x	x	x								x	
	p165		serpentinite									x		x	x							x	
Transect G	n50	Galissas	block Fe-Ti	x			x	x	x			x				x			x		x	x	37.4306/24.8818
	n30		block Fe-Ti	x			x	x	x			x				x			x			x	
	n8		rind	x			x	x	x			x				x			x				
	n8b		rind	x			x	x	x			x	x			x	x		x				
	n2		rind									x				x	x		x			x	
	p1		matrix									x	x									x	
	p30		matrix									x		x								x	
Transect K (18)	18a	Kini	block Fe-Ti	x			x	x			x	x				x	x					x	37.4439/24.8890
	18b		rind	x			x	x			x	x				x	x						
	18c		matrix									x	x			x	x						
	18d		rind	x			x	x				x				x	x					x	
	18e		rind	x			x	x			x	x				x	x						
Transect 9	9a	Lia	block Mg-Al			x	x	x	x		x	x				x	x		x			x	37.4924/24.9089
	9b		block Mg-Al			x	x	x	x		x	x				x	x		x			x	

	9c		rind				x		x	x		x	x					x	x		x				
	9d		rind				x						x					x	x						
Transect 19	19a	Lia	block Fe-Ti	x			x	x		x	x		x					x	x	x	x			x	37.4914/24.9072
	19b		block Fe-Ti	x			x	x		x			x					x	x						
	19c		rind				x						x						x						
others	581	Galissas	Serpentinite										x				x								37.4311/24.8820
	582	Galissas	block Fe-Ti	x			x		x				x					x	x						37.4311/24.8820
	4	Galissas	block Fe-Ti	x			x	x	x	x			x					x	x					x	37.4316/24.8819
	17	Lia	dyke siliceux					x			x	x	x							x	x			x	37.4923/24.9088
	21	Lia	Fe-Ti block rind				x	x	x	x			x						x			x		x	37.4902/24.9015
	22	Lia	metavolcanic rind				x	x	x	x		x						x	x						37.4916/24.9006
	23	Lia	Fe-Ti block rind										x	x				x	x		x				37.4916/24.9006
	24	Lia	metavolcanic rind		x		x	x				x	x	x				x	x						37.4921/24.9011
	27	Lia	Fe-Ti block rind	x			x	x	x	x		x	x					x	x					x	37.4918/24.9213

1277

1278 *Table 1: Samples nature, mineralogy and localization.*

1279

	Transect L								Transect G						
Samples	**n290**	**n57**	**n10**	**n1**	**p5**	**p125**	**p135**	**p165**	**n50**	**n30**	**n8**	**n2**	**p1**	**p30**	**s581**
B	8,1	5,4	7,9	22,1	4,9	2	3,9	4,8	8,2	5,3	4,2	2,7	8,3	4,4	5,2
Li	34,4	15,3	45,5	31,8	10,4	0,95	0,89	0,92	18,1	20,4	22,3	5,49	1,1	1,21	5,37
As	0,93	0,59	-	1,45	-	-	-	1,13	1,50	0,81	0,50	1,16	0,54	0,87	0,74
Ba	105	53,2	84,4	195	-	-	-	-	14,5	-	-	-	-	-	-
Be	0,60	0,43	0,73	0,93	1,08	0,09	0,79	0,44	0,85	0,80	0,61	0,15	0,77	-	0,05
Bi	0,21	0,07	0,05	0,10	-	-	-	-	-	-	-	-	-	-	-
Cd	0,56	0,21	0,15	0,08	0,17	0,02	0,18	0,05	0,17	0,18	0,13	0,05	0,16	-	-
Co	30,9	16,7	40,0	26,8	64,0	78,0	80,0	93,3	41,2	34,5	30,2	91,0	51,0	90,4	88,6
Cr	244	85,0	27,9	82,8	1715	1923	1182	3329	24,1	21,9	10,3	64,3	1840	2755	1849
Cs	0,99	0,28	0,98	2,13	0,02	-	-	0,02	0,22	0,17	0,21	-	-	0,36	-
Cu	32,6	30,5	6,0	57,0	13,2	13,3	15,7	38,5	18,4	4,9	7,3	18,7	9,1	15,9	42,3
Ga	18,2	20,7	12,7	16,6	9,44	4,29	4,26	5,68	17,4	15,3	15,1	16,2	3,61	4,11	4,21
Ge	1,52	1,60	1,10	0,90	1,08	1,05	1,36	0,84	1,33	1,31	1,12	0,91	1,28	1,10	0,83
Hf	3,23	3,81	2,34	3,26	3,82	1,16	2,00	-	2,75	3,17	1,89	5,84	0,05	-	-
In	0,13	0,10	0,05	0,09	0,05	-	-	-	0,10	0,10	0,15	0,04	0,06	-	-
Nb	6,52	3,75	1,94	2,13	1,90	0,32	3,00	0,43	6,39	6,13	2,15	5,55	0,03	0,03	0,07
Ni	81,5	24,9	71,0	57,4	1238	1654	1389	2068	45,8	36,5	30,0	586	1456	1785	1806
Pb	8,15	5,15	4,52	3,30	0,93	-	0,84	-	2,62	2,01	0,94	-	0,52	-	-
Rb	17,9	5,95	16,1	36,6	0,19	-	-	-	2,31	0,57	0,83	-	0,16	3,65	0,34
Sb	0,15	0,12	0,12	0,17	-	-	0,07	0,07	0,10	0,06	0,08	0,11	-	-	-
Sc	34,88	26,34	30,15	34,85	14,90	3,51	35,83	17,65	38,09	36,05	54,51	25,90	27,47	2,21	10,78
Sn	1,00	1,05	0,78	1,31	1,61	-	0,62	1,77	1,82	1,59	1,33	0,91	0,44	-	0
Sr	325	366	164	117	8,9	1,6	12,5	2,5	189	327	245	22,5	22,2	-	1,9
Ta	0,34	0,30	0,12	0,16	0,21	0,04	0,23	0,16	0,52	0,49	0,17	0,63	-	-	0,01
Th	3,26	5,23	1,89	2,73	0,43	0,40	0,16	0,11	0,24	0,25	0,19	0,43	-	-	0,05
U	0,90	1,03	0,54	1,19	0,17	0,03	0,13	0,03	0,14	0,13	0,07	0,14	-	-	0,01
V	233	209	219	264	97,3	40,7	69,8	83,0	508	457	394	460	156	75,3	83,6
Y	37,9	33,6	20,0	42,0	22,0	2,21	20,6	2,70	45,5	46,1	42,3	52,6	18,7	0,14	1,42
Zn	201	77,0	169	66,7	79,4	51,0	48,6	70,7	141	112	86,6	133	57,1	63,4	95,9
Zr	122	138	79,8	115	159	43,6	66,8	-	105	139	65,8	258	1,62	-	-
La	14,5	14,2	6,08	10,4	3,96	2,34	0,752	0,103	5,64	4,97	5,06	9,69	0,079	0,032	0,025
Ce	33,9	32,6	14,9	25,2	10,8	5,42	3,11	0,347	17,8	15,9	15,3	40,2	0,511	0,055	0,061
Pr	4,57	4,30	2,19	3,67	1,57	0,669	0,640	0,079	2,99	2,75	2,68	7,12	0,176	0,013	0,017
Nd	20,9	19,6	10,3	17,4	7,29	2,63	3,74	0,385	16,5	15,2	15,0	36,9	1,45	0,062	0,113
Sm	5,56	5,05	2,94	5,16	2,24	0,432	1,78	0,174	5,34	5,09	5,17	10,5	1,05	0,019	0,066
Eu	1,74	1,74	0,969	1,94	0,531	0,065	0,328	0,026	2,59	2,32	1,39	3,11	0,233	0,004	0,019
Gd	5,91	5,36	3,17	6,12	2,73	0,371	2,56	0,209	6,31	6,01	6,23	10,4	1,80	0,021	0,145
Tb	0,998	0,898	0,538	1,09	0,509	0,054	0,535	0,049	1,15	1,13	1,14	1,61	0,412	0,004	0,023
Dy	6,60	5,73	3,55	7,42	3,65	0,339	3,79	0,369	7,78	7,87	7,69	9,67	3,10	0,026	0,167
Ho	1,47	1,29	0,790	1,65	0,827	0,078	0,847	0,085	1,74	1,75	1,68	1,98	0,685	0,006	0,046
Er	4,08	3,55	2,20	4,40	2,33	0,247	2,30	0,251	4,71	4,76	4,36	5,24	1,92	0,014	0,144
Tm	0,620	0,555	0,341	0,629	0,374	0,041	0,345	0,0453	0,717	0,720	0,641	0,743	0,288	0,0024	0,0246
Yb	3,96	3,61	2,22	3,89	2,43	0,298	2,06	0,325	4,61	4,52	3,94	4,67	1,83	0,017	0,163
Lu	0,611	0,560	0,346	0,589	0,378	0,054	0,283	0,054	0,722	0,687	0,608	0,771	0,249	0,003	0,036
SiO2	49,09	56,56	53,32	52,89	48,14	54,45	50,33	43,44	43,19	45,43	45,13	26,83	53,30	54,62	45,11
Al2O3	15,88	14,92	12,61	14,75	6,14	2,67	3,44	2,99	13,36	12,04	10,96	15,12	2,52	2,07	2,03
Fe2O3	11,20	9,26	11,47	10,70	8,36	6,50	7,70	10,19	16,36	14,82	12,02	16,83	7,04	7,58	8,15
MnO	0,29	0,31	0,18	0,081	0,19	0,039	0,16	0,13	0,25	0,24	0,16	0,32	0,19	0,036	0,12
MgO	6,55	3,01	8,56	7,21	21,71	28,89	24,83	31,07	5,87	6,45	11,02	21,56	21,31	28,70	33,00
CaO	7,76	9,57	3,96	2,42	8,16	0,07	6,37	0,05	7,83	9,45	9,02	3,13	9,91	0,07	0,05
Na2O	4,09	2,08	5,68	5,91	0,88	-	0,25	-	5,54	5,89	5,10	-	1,22	-	-
K2O	0,86	0,37	0,60	1,34	0,05	-	-	-	0,11	-	-	-	0,09	-	-
TiO2	1,20	1,25	1,09	1,32	0,40	0,066	0,69	0,085	4,58	3,66	1,51	6,51	0,020	0,039	-
P2O5	0,29	0,27	-	0,22	-	-	0,16	-	-	-	0,41	0,55	-	-	-

PF	1,96	1,92	1,70	2,58	4,97	6,17	4,90	10,33	1,94	1,70	3,51	8,93	3,27	5,29	10,31

1280

1281 *Table 2: Samples whole-rock major (%) and trace element (µg/g) concentrations.*

1282

	Amp		Chl		Grt				Cpx		Ep	Ph		Srp	Tlc	Tur
Sample	L_n10	L_p135	L_n10	L_p135	L_n57	L_n57	K_18e	K_18e	G_n8	4	L_n10	L_n10	17	L_p165	L_p165	21
Location	rind	matrix	rind	matrix	core	rim	core	rim	rind	peak	rind	rind	block	matrix	matrix	rind
SiO2	58,15	58,01	26,60	31,50	37,82	38,14	37,88	36,62	55,27	56,12	38,64	51,78	47,31	41,23	60,91	37,57
TiO2	0,03	0,02	0,06	0,02	0,19	0,10	0,07	0,17	0,12	0,07	0,07	0,15	0,03	0,01	0,02	0,53
Al2O3	10,52	0,56	18,94	16,68	20,94	21,44	21,42	20,92	6,80	10,16	26,41	26,37	39,78	2,81	0,37	31,77
Cr2O3	0,01	0,01	0,00	0,00	0,15	0,15	0,01	0,00	0,00	0,02	0,00	0,00	0,00	0,43	0,11	0,07
FeO	10,81	5,97	25,09	10,31	25,45	28,63	26,63	19,64	9,41	6,98	9,91	2,94	0,23	10,73	3,40	5,03
MnO	0,14	0,23	0,77	0,11	4,41	0,90	1,11	10,22	0,20	0,01	0,22	0,03	0,00	0,17	0,03	0,00
MgO	10,74	20,66	15,84	28,66	1,89	3,08	2,84	1,43	8,60	7,05	0,00	3,65	0,03	31,83	29,12	8,49
CaO	0,93	12,43	0,03	0,00	9,86	8,66	10,06	10,44	13,65	11,91	23,24	0,02	0,12	0,00	0,05	0,29
Na2O	7,27	0,51	0,02	0,03	0,00	0,00	0,03	0,00	6,65	7,97	0,02	0,49	7,65	0,01	0,03	2,95
K2O	0,02	0,02	0,11	0,00	0,00	0,01	0,00	0,00	0,01	0,01	0,02	9,69	0,35	0,00	0,05	0,03
Total	98,63	98,41	87,41	87,31	100,62	101,07	100,03	99,44	100,91	100,30	98,77	95,07	95,51	87,21	94,09	86,72
O	23	23	14	14	24	24	24	24	6	6	12,5	11	11	7	11	29
Si	7,95	8,00	2,82	3,06	5,99	5,98	5,90	5,98	2,01	2,01	3,07	3,45	3,01	2,00	3,97	6,05
Ti	0,00	0,00	0,00	0,00	0,02	0,01	0,02	0,01	0,00	0,00	0,00	0,01	0,00	0,00	0,00	0,06
Al	1,70	0,09	2,37	1,91	3,91	3,96	3,98	3,99	0,29	0,43	2,47	2,07	2,98	0,16	0,03	6,03
Cr	0,00	0,00	0,00	0,00	0,02	0,02	0,00	0,00	0,00	0,00	0,00	0,00	0,00	0,02	0,01	0,01
Fe tot	1,24	0,69	2,22	0,84	3,37	3,75	2,65	3,52	0,29	0,21	0,66	0,16	0,01	0,44	0,19	0,68
Mn	0,02	0,03	0,07	0,01	0,59	0,12	1,40	0,15	0,01	0,00	0,01	0,00	0,00	0,01	0,00	0,00
Mg	2,19	4,25	2,50	4,15	0,45	0,72	0,34	0,67	0,47	0,38	0,00	0,36	0,00	2,31	2,83	2,04
Ca	0,14	1,84	0,00	0,00	1,67	1,46	1,80	1,70	0,53	0,46	1,98	0,00	0,01	0,00	0,00	0,05
Na	1,93	0,14	0,00	0,01	0,00	0,00	0,00	0,01	0,47	0,55	0,00	0,06	0,94	0,00	0,00	0,92
K	0,00	0,00	0,01	0,00	0,00	0,00	0,00	0,00	0,00	0,00	0,00	0,82	0,03	0,00	0,00	0,01
Fe3+	0,17	0,04	0,01	0,00	0,08	0,04	0,12	0,03	0,18	0,12	0,66	0,04	0,00		0,02	
Fe2+	1,07	0,65	2,21	0,84	3,29	3,71	2,53	3,49	0,11	0,08	0,00	0,13	0,01		0,17	
Comp.	Gln	Act	Daph37.8	Daph16.4	Grs25.4	Grs22.7	Grs23.5	Grs26.7	Jd27.9	Jd42.3	Pi58.2	Tri6	Tri1.1			
			Clin42.6	Clin81.4	Prp7.4	Prp12	Prp10.3	Prp5.6	Ae17	Ae12.3	Zo41.8	Prl11.1	Prl2.7			
			Am16.2	Am0	Alm54.8	Alm61.8	Alm58.3	Alm41.6	Quad55.1	Quad45.5		Ms41.8	Ms34.5			
			Sud2.7	Sud2.2	Sps9.9	Sps2	Sps6.1	Sps23				Cel34.6	Cel0			
					Adr2	Adr1.1	Adr1.8	Adr3.1								

1283

1284 *Table 3: Representative EMPA analyses (wt.%) of minerals in the reaction zones.*

1285

1286 **Figure Captions**

1287 *Figure 1: Geological maps of Syros, after (Laurent et al., 2016) and (Keiter et al., 2011), with*

1288 *localization of samples. mv: metavolcanic, mg: metagabbro, mr: marble, sp: serpentinite and*

1289 *msch: micaschists.*

Figure 2: (a) Satellite picture of the Kampos-Lia mélange zone with various field observations. Histograms of blocks (b) length-to-width ratio and (c) volume. The 'other' category correspond to mixte Fe-Ti and Mg-Al, metavolcanic or carbonate blocks. (d) Folded garnets layers from the Lia shear zone. (e) Nature and localization of blocks. (f) Geological map of the Kampos-Lia mélange zone with orientation of the blocks elongation axe.

Figure 3: Deformation in the Kampos-Lia mélange zone. Metric (a, b) to centimetric (c) folds in metavolcanic layers characterized by sub-horizontal W-E axes. (d) Folded succession of metavolcanic layer, glaucophane-rich rind and tremolite-rich matrix. (e) Asymmetric boudinage and folds in a metavolcanic layer compatible with top-to-the east shearing. (f) Rounded metabasite block in a matrix top-to-the east shear band. (g) Asymmetric boudinage of a metabasite layer in marble with top-to-the east shearing deformation. Sheath folds (h) and asymmetric boudinage (i) of garnet rich layer associated with chlorite crystallization along the Lia Shear zone.

Figure 4: (a) Panorama of the Kampos-Lia mélange zone with (b) WE cross-section and (c) 3D block diagram.

Figure 5: Localization of the samples from transect L.

Figure 6: Field pictures. Diversity of block-rind-matrix associations and mineralogic assemblages. (a-f) metavolcanic layers, (g-j) Fe-Ti rich blocks, (k) Mg-Al rich blocks, (l) Block of intermediate composition with associated rind and/or matrix.

Figure 7: Rind systematics for the three major block and layer lithologies with microphotographs of representative samples from (a,b) Metavolcanic layer, (d,e,g,h,i) Fe-Ti rich block, (j,k,l) Mg-Al rich block and (c,f) matrix.

Figure 8: Whole rock compositions of samples from transects L and G represented against distance from the contact block/matrix. Double arrows to the side of the plot showing Al_2O_3 concentration for transect L show the variation of initial compositions in Aluminum based on our own data (samples L_n290, L_n57, L_p165 and 581) , metavolcanics (zones I and II) from Pogge von Strandmann et al. (2015) and unmetasomatized serpentinite from Cooperdock et al. (2018).

Figure 9: Whole rock compositions from transects L, G and 581. (a) Th/La vs Sm/La diagram after Plank (2005). (b) CaO vs MgO diagram with data compilation from Miller et al. (2009) for reference. Harz: harzburgites (GEOROC database, MPI für Chemie, Mainz), AOC: altered oceanic crust (Kelley et al., 2003), New Cal: New Caledonia (Spandler et al., 2008) and Catalina mélange (King et al., 2006). The five zones of a reaction zone studied by Miller et al. (2009) are connected from zone 1 to 5 (Miller et al., 2009). (c) Chondrite normalized Cr vs Eu anomalies (Eu/Eu) diagram. (d, e, f) Cr vs Al_2O_3, TiO_2 and Zr diagrams. (g, h) Multi-element diagrams normalized to chondrite (Sun and McDonough, 1989). Reference spectra are MORB (McDonough and Sun, 1995) and Syros serpentinites (Cooperdock et al., 2018).*

Figure 10: Mass ratio of whole rock compositions. (a) Element mobility in transect L along the contact block/matrix during fluid rock interaction. Mass ratio of metasomatic matrix to serpentinite (p5/p165) against mass ratio of rind to metavolcanic (n1/n57). Metasomatic samples compositions are normalized to the protolith Al content. (b) Mass ratio of metasomatic

matrix to serpentinite (p125/p165) in transect L. As and Sb are below detection limit only in L_p165. Hf and Zr are below detection limit only in L_p125. (c) Mass ratio of metasomatic matrix to serpentinite (p5/p165) in transect L. Hf, In, Pb, Rb, Zr, Na2O and K2O content are below detection limit only in L_p165 . As and Sb are below detection limit only in L_p5. (d) Mass ratio of rind to metavolcanic (n1/n57) in transect L. (e) Mass ratio of rind to Fe-Ti block (n2/n50) in transect G. Ba, Cs, Pb, Rb, Na and K are below detection limit only in G_n2.

Figure 11: (a) Composition of amphiboles in a XNa (Na/(Na+Ca)) vs XMg (Mg/(Fe+Mg)) diagram with an X-ray compositional map of tremolites from L_p135 .(b) Composition of chlorites in a 2Al vs XMg diagram with two Si vs XMg diagrams for transects G and L.

Figure 12: (a) Composition of clinopyroxenes in a Ca vs XMg diagram and a Di+Hd-Aeg+Jd ternary diagram. (b) Composition of garnets in a Sps+Grs-Alm-Prp ternary diagram. (c) Composition of phengites in a 2Al vs XMg diagram.(d) X-ray compositional map of a garnet from L_n290.

Figure 13: (a-g) Chondrite normalized trace element profiles for minerals from samples from transect L and G. (h) Chondrite-normalized Cr vs Eu anomalies (Eu/Eu) diagram for garnets. Chondrite normalization data after Sun and McDonough (1989).*

Figure 14: Trace element compositions of amphiboles, chlorites and clinopyroxenes in transect L, G and K.(a) Cr vs Li,(b) Cr vs Ni and (c) Cr vs Co diagrams.

Figure 15: Schematic diagrams showing the diversity of the block-matrix-fluid compositions and interactions in Syros mélange zones.

Figure 16: (a) Summary of P-T paths proposed by different researchers for Syros with estimated P-T conditions for metasomatism. (b) Conceptual view of the Kampos-Lia mélange zone during exhumation .(c) Schematic representation of the elements exchange during metasomatism in the Kampos-Lia mélange zone with lithologies representativity.

Figure 17: Three stage conceptual views of the Kampos-Lia mélange zone during the tectonometamorphic evolution of the CBU

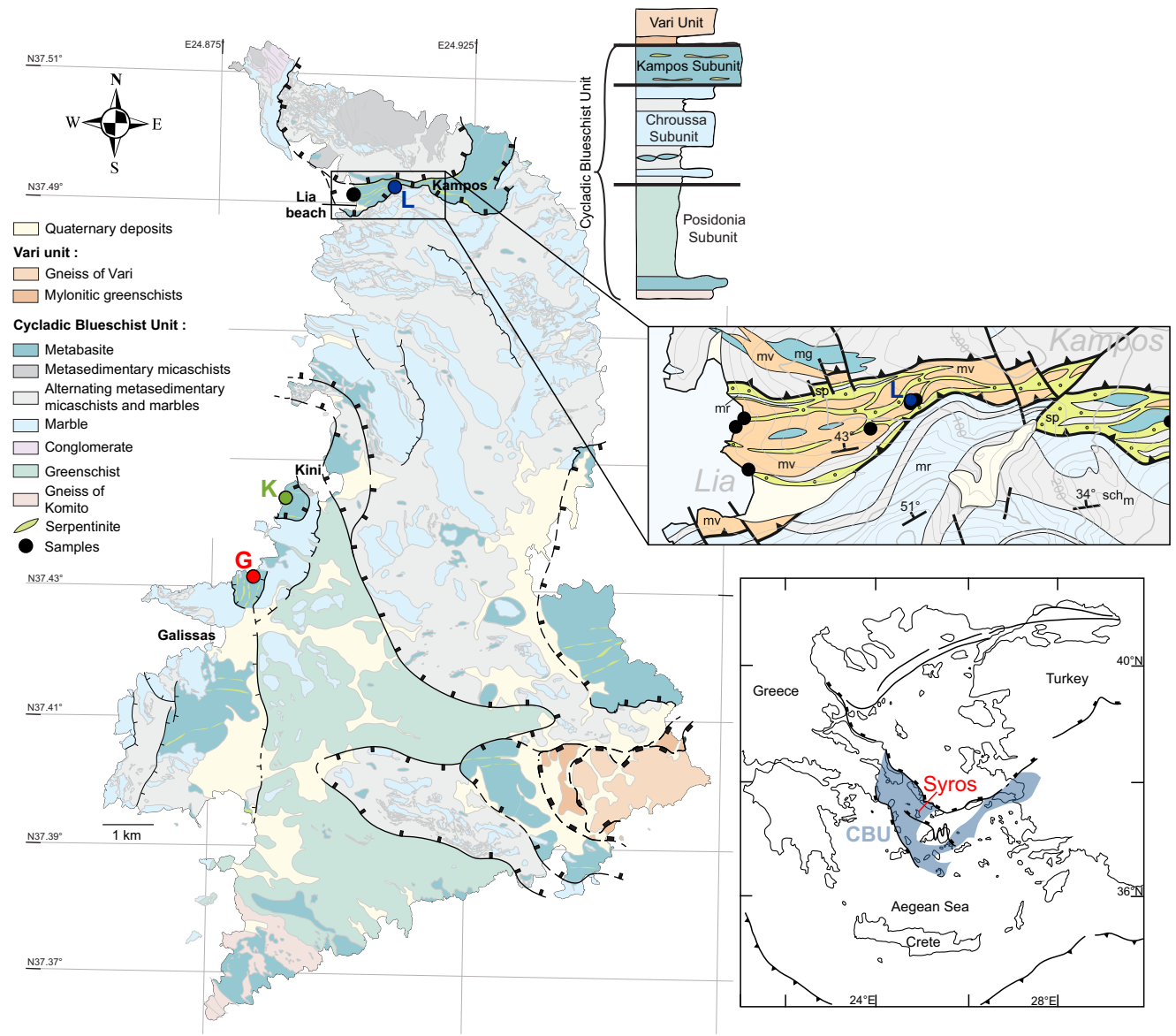
E24.875
E24.925
N37.51°
N37.49°
N37.43°
N37.41°
N37.39°
N37.37°
N
W
E
S
Lia beach
L
Kampos
Kini
K
G
Galissas
1 km
Quaternary deposits
Vari unit :
Gneiss of Vari
Mylonitic greenschists
Cycladic Blueschist Unit :
Metabasite
Metasedimentary micaschists
Alternating metasedimentary micaschists and marbles
Marble
Conglomerate
Greenschist
Gneiss of Komito
Serpentinite
Samples
Vari Unit
Kampos Subunit
Chroussa Subunit
Posidonia Subunit
Cycladic Blueschist Unit
Kampos
Lia
mv
mg
sp
mr
43°
51°
34°
schm
Greece
Turkey
Syros
CBU
Aegean Sea
Crete
40°N
36°N
24°E
28°E

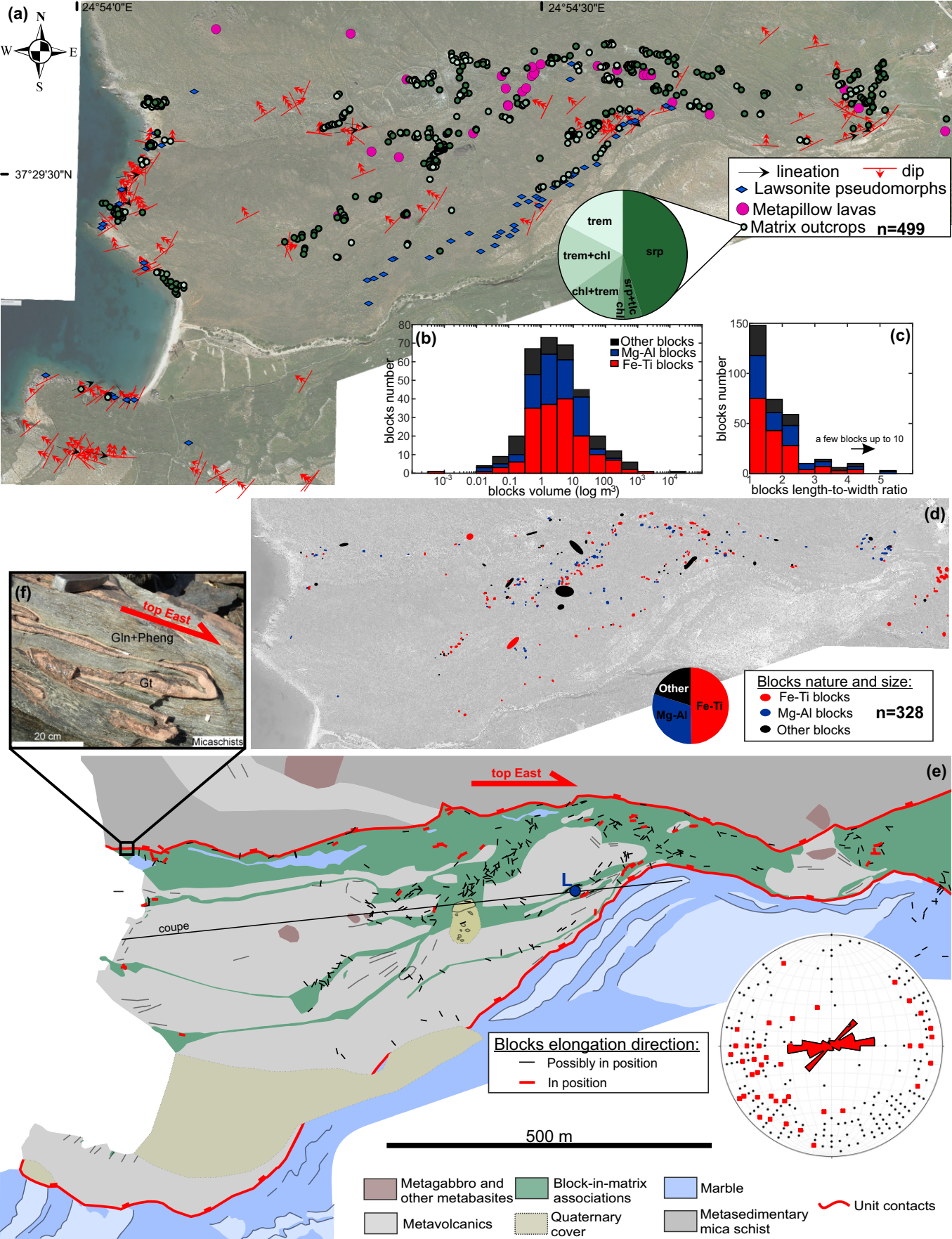
(a)
N
W
E
S
24°54'0"E
24°54'30"E
37°29'30"N
lineation
dip
Lawsonite pseudomorphs
Metapillow lavas
Matrix outcrops n=499
trem
trem+chl
chl+trem
srp
srp+tlc
chl
(b)
Other blocks
Mg-Al blocks
Fe-Ti blocks
blocks number
blocks volume (log m3)
(c)
blocks number
a few blocks up to 10
blocks length-to-width ratio
(d)
Other
Mg-Al
Fe-Ti
Blocks nature and size:
Fe-Ti blocks
Mg-Al blocks
Other blocks
n=328
(f)
top East
Gln+Pheng
Gt
20 cm
Micaschists
(e)
top East
L
coupe
Blocks elongation direction:
Possibly in position
In position
500 m
Metagabbro and other metabasites
Block-in-matrix associations
Marble
Unit contacts
Metavolcanics
Quaternary cover
Metasedimentary mica schist

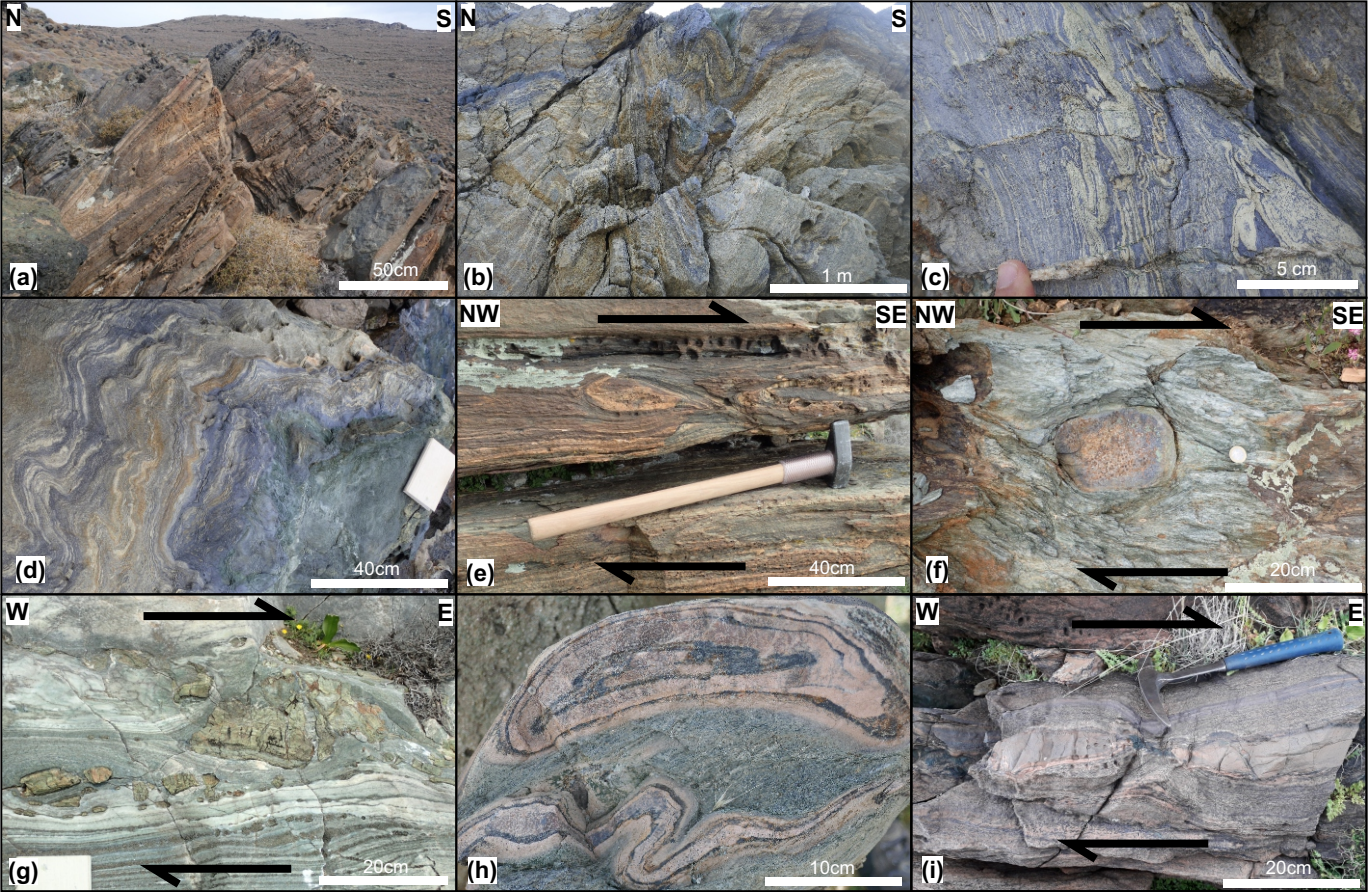
N
S
(a)
50cm
N
S
(b)
1 m
(c)
5 cm
(d)
40cm
NW
SE
(e)
40cm
NW
SE
(f)
20cm
W
E
(g)
20cm
(h)
10cm
W
E
(i)
20cm

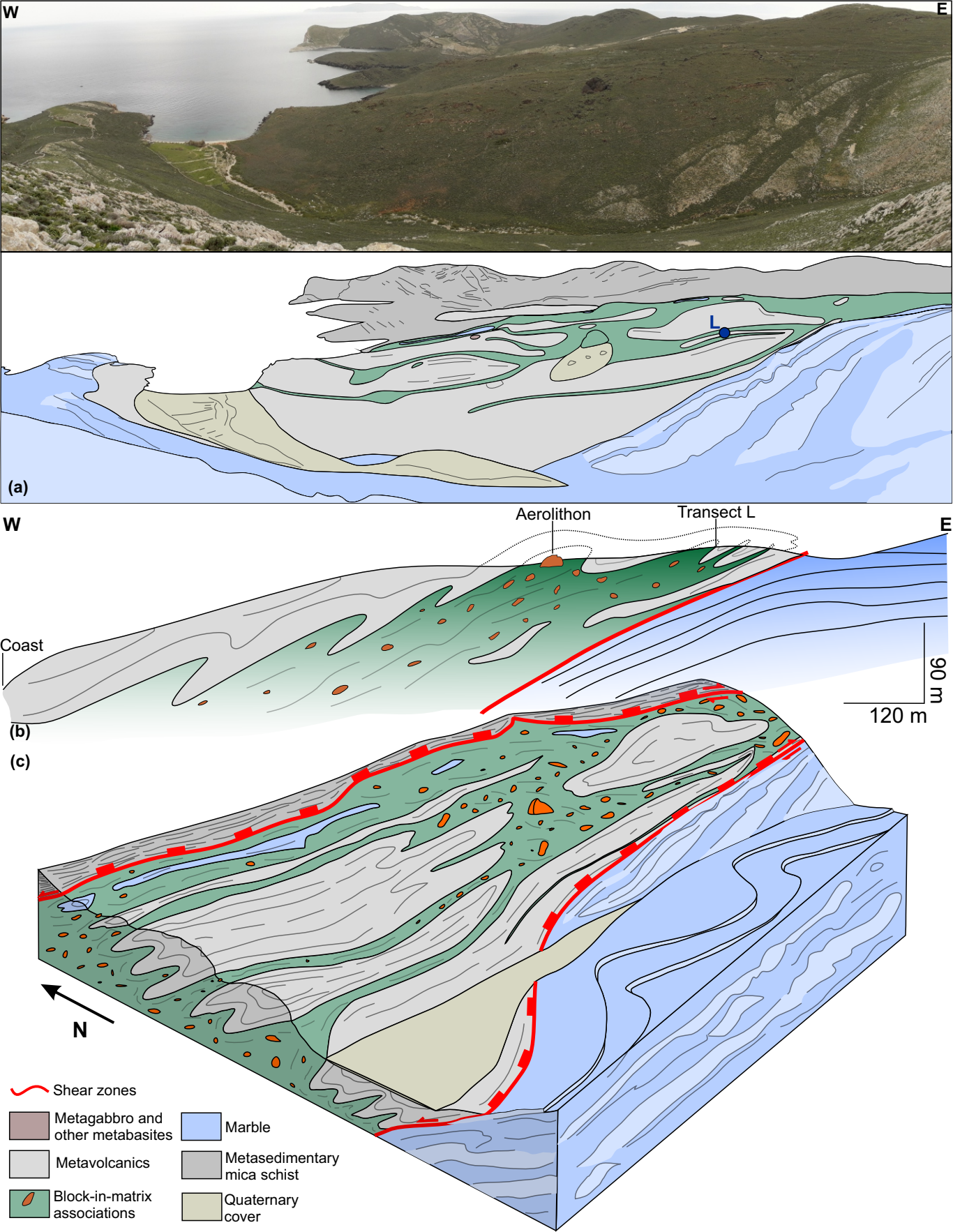
W
E
L
(a)
W
Aerolithon
Transect L
E
Coast
90 m
120 m
(b)
(c)
N
Shear zones
Metagabbro and other metabasites
Marble
Metavolcanics
Metasedimentary mica schist
Block-in-matrix associations
Quaternary cover


Transect L
p165
p135
p125
p5
n1
n10
n57
n290

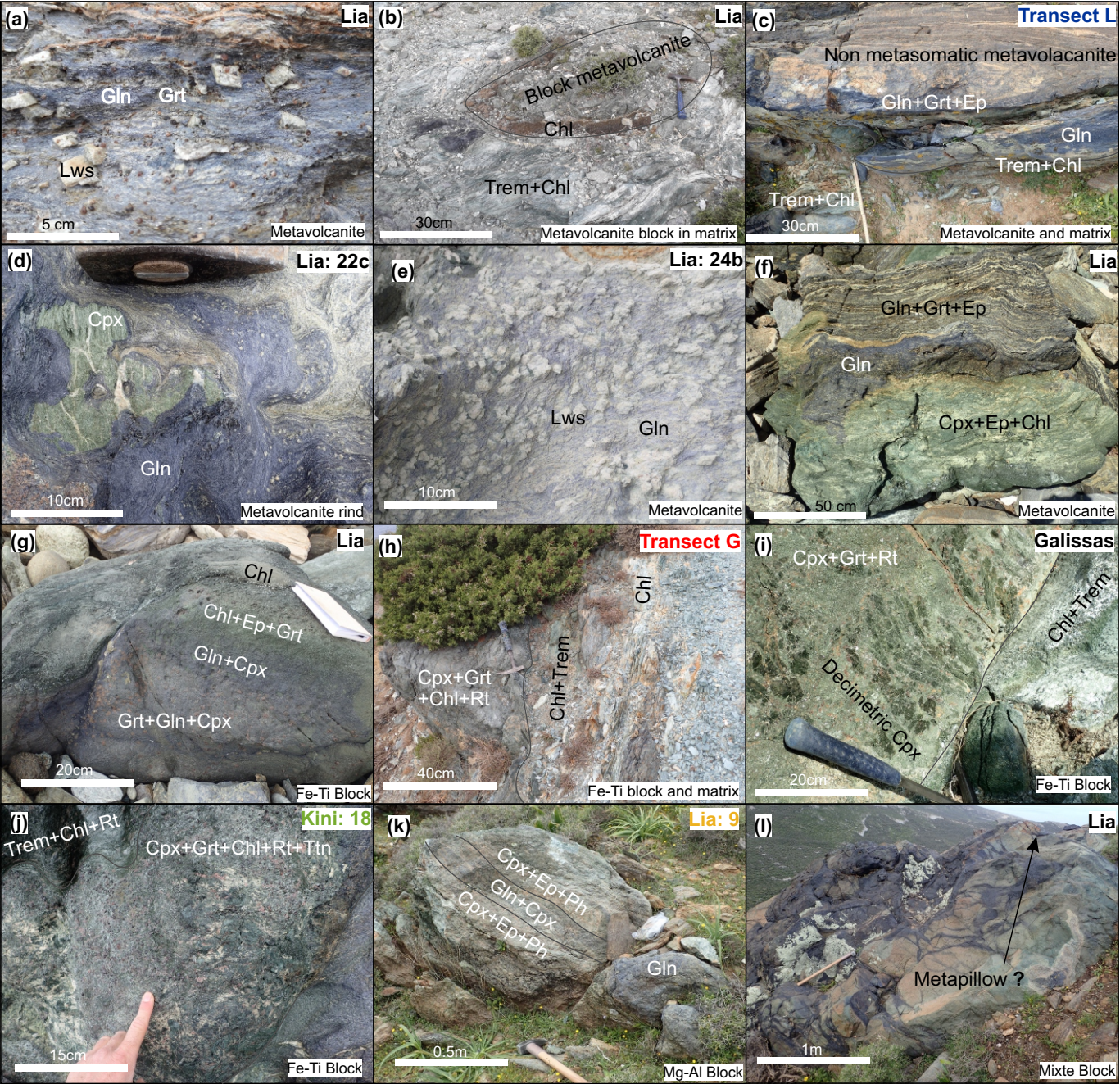
(a)
Lia
Gln
Grt
Lws
5 cm
Metavolcanite
(b)
Lia
Block metavolcanite
Chl
Trem+Chl
30cm
Metavolcanite block in matrix
(c)
Transect L
Non metasomatic metavolacanite
Gln+Grt+Ep
Gln
Trem+Chl
Trem+Chl
30cm
Metavolcanite and matrix
(d)
Lia: 22c
Cpx
Gln
10cm
Metavolcanite rind
(e)
Lia: 24b
Lws
Gln
10cm
Metavolcanite
(f)
Lia
Gln+Grt+Ep
Gln
Cpx+Ep+Chl
50 cm
Metavolcanite
(g)
Lia
Chl
Chl+Ep+Grt
Gln+Cpx
Grt+Gln+Cpx
20cm
Fe-Ti Block
(h)
Transect G
Chl
Chl+Trem
Cpx+Grt
+Chl+Rt
40cm
Fe-Ti block and matrix
(i)
Galissas
Cpx+Grt+Rt
Chl+Trem
Decimetric Cpx
20cm
Fe-Ti Block
(j)
Kini: 18
Trem+Chl+Rt
Cpx+Grt+Chl+Rt+Ttn
15cm
Fe-Ti Block
(k)
Lia: 9
Cpx+Ep+Ph
Gln+Cpx
Cpx+Ep+Ph
Gln
0.5m
Mg-Al Block
(l)
Lia
Metapillow ?
1m
Mixte Block

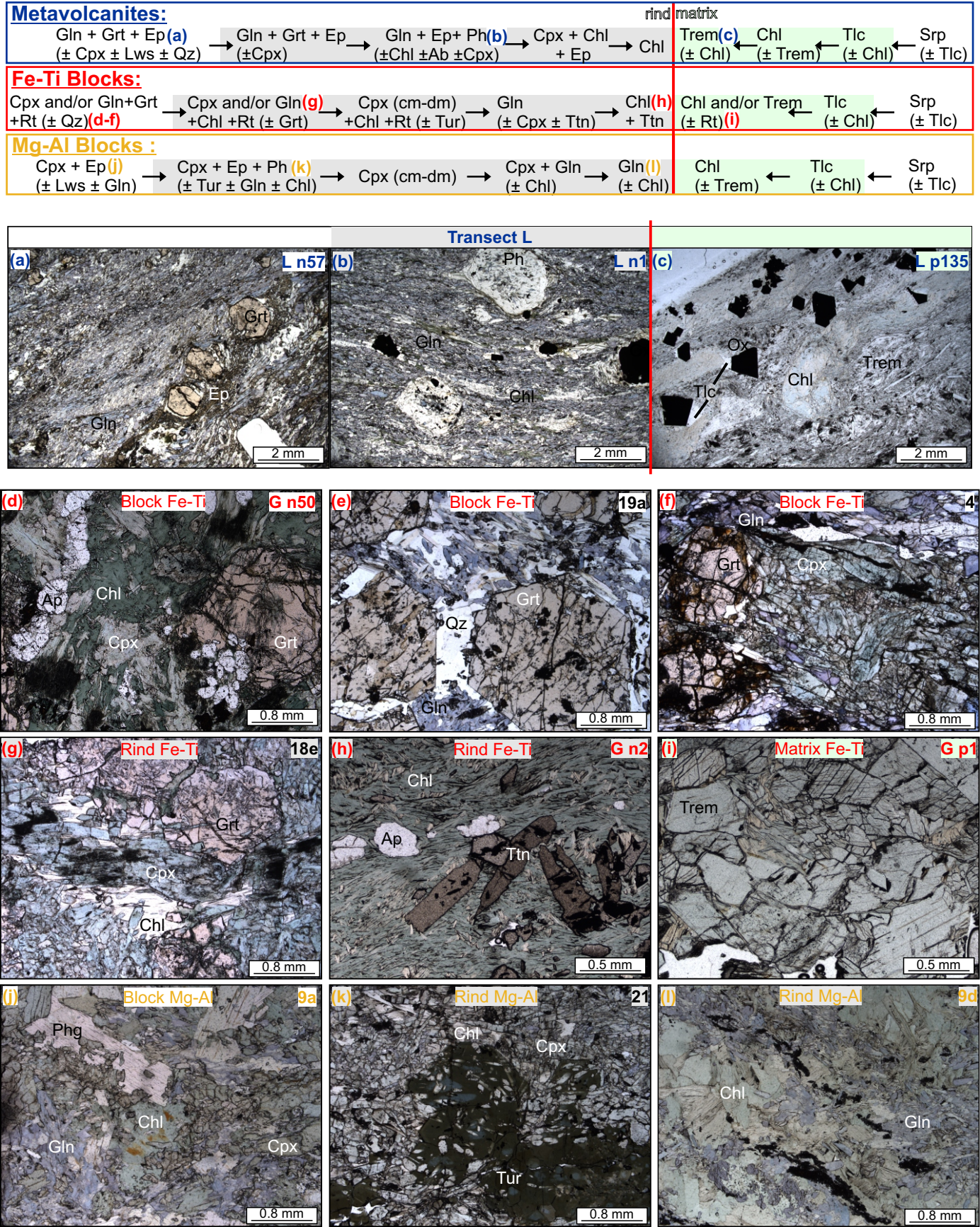
Metavolcanites:
rind
matrix
Gln + Grt + Ep (a) (± Cpx ± Lws ± Qz)
Gln + Grt + Ep (±Cpx)
Gln + Ep+ Ph (b) (±Chl ±Ab ±Cpx)
Cpx + Chl + Ep
Chl
Trem (c) (± Chl)
Chl (± Trem)
Tlc (± Chl)
Srp (± Tlc)
Fe-Ti Blocks:
Cpx and/or Gln+Grt +Rt (± Qz) (d-f)
Cpx and/or Gln (g) +Chl +Rt (± Grt)
Cpx (cm-dm) +Chl +Rt (± Tur)
Gln (± Cpx ± Ttn)
Chl (h) + Ttn
Chl and/or Trem (± Rt) (i)
Tlc (± Chl)
Srp (± Tlc)
Mg-Al Blocks :
Cpx + Ep (j) (± Lws ± Gln)
Cpx + Ep + Ph (k) (± Tur ± Gln ± Chl)
Cpx (cm-dm)
Cpx + Gln (± Chl)
Gln (l) (± Chl)
Chl (± Trem)
Tlc (± Chl)
Srp (± Tlc)
Transect L
(a)
L n57
Grt
Ep
Gln
2 mm
(b)
L n1
Ph
Gln
Chl
2 mm
(c)
L p135
Ox
Trem
Chl
Tlc
2 mm
(d)
Block Fe-Ti
G n50
Ap
Chl
Cpx
Grt
0.8 mm
(e)
Block Fe-Ti
19a
Grt
Qz
Gln
0.8 mm
(f)
Block Fe-Ti
4
Gln
Grt
Cpx
0.8 mm
(g)
Rind Fe-Ti
18e
Grt
Cpx
Chl
0.8 mm
(h)
Rind Fe-Ti
G n2
Chl
Ap
Ttn
0.5 mm
(i)
Matrix Fe-Ti
G p1
Trem
0.5 mm
(j)
Block Mg-Al
9a
Phg
Chl
Gln
Cpx
0.8 mm
(k)
Rind Mg-Al
21
Chl
Cpx
Tur
0.8 mm
(l)
Rind Mg-Al
9d
Chl
Gln
0.8 mm

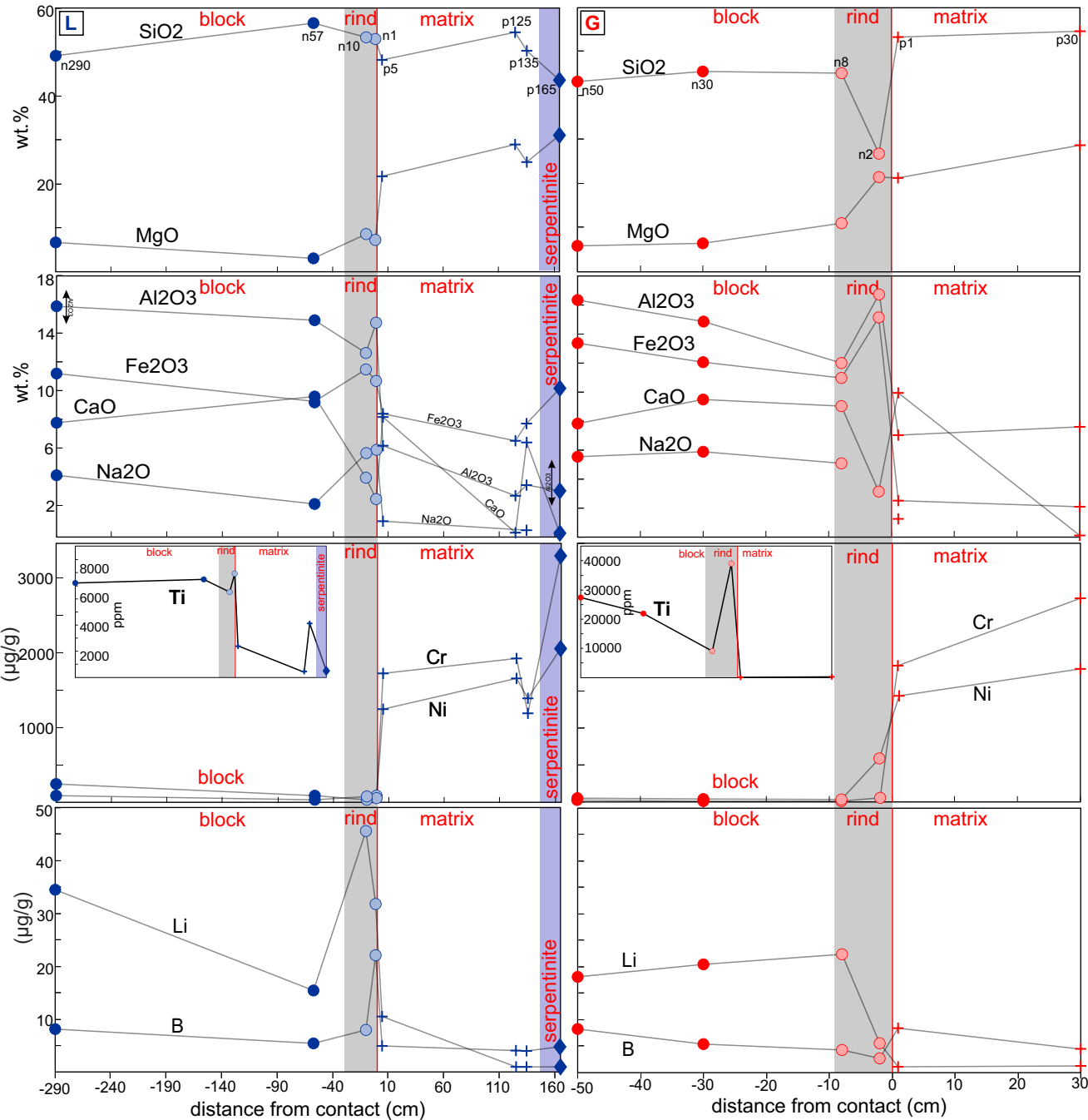
L
G
block
rind
matrix
serpentinite
SiO2
MgO
Al2O3
Fe2O3
CaO
Na2O
Ti
Cr
Ni
Li
B
wt.%
(µg/g)
ppm
n290
n57
n10
n1
p5
p125
p135
p165
n50
n30
n8
n2
p1
p30
distance from contact (cm)

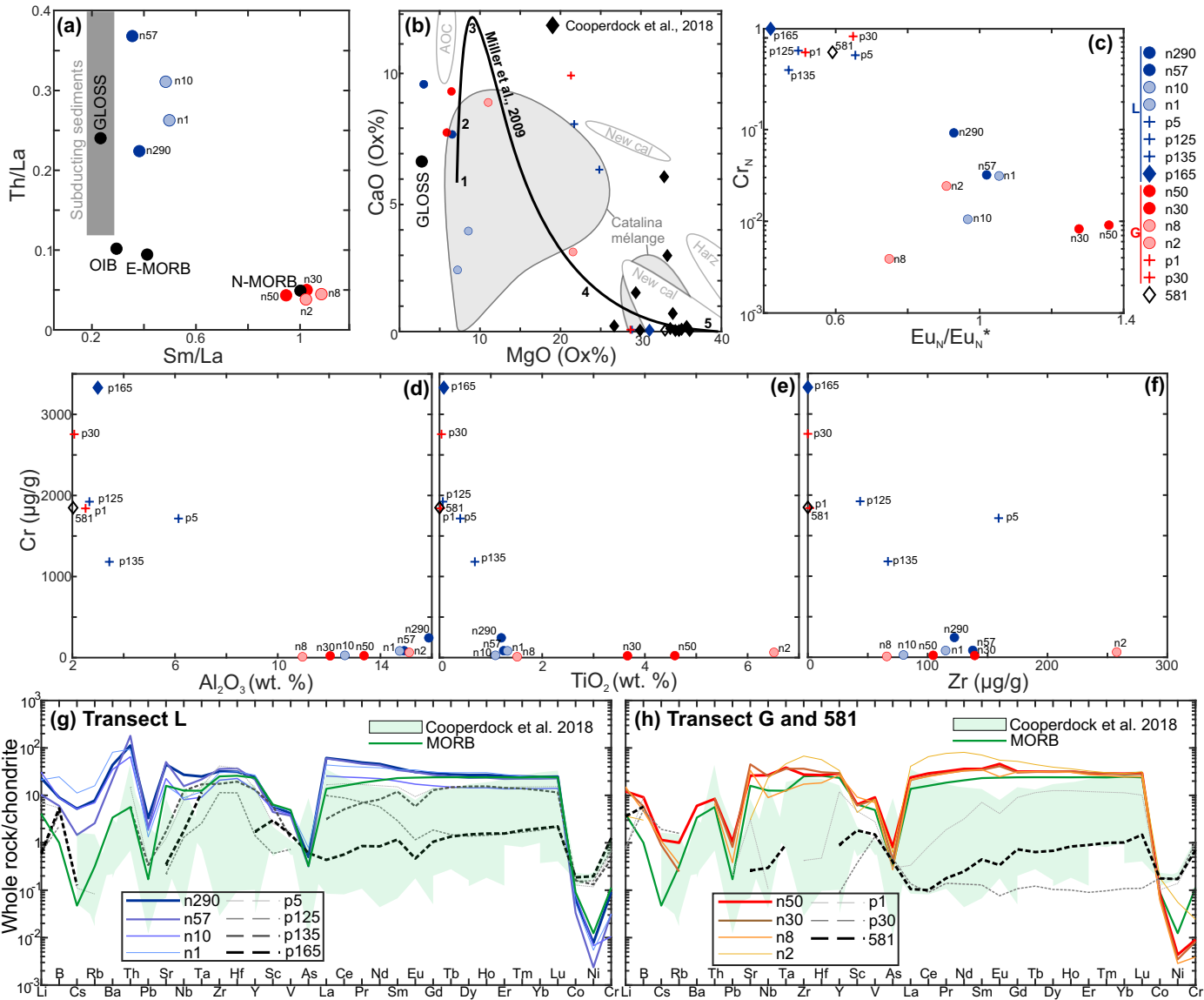
(a)
Th/La
Sm/La
Subducting sediments
GLOSS
n57
n10
n1
n290
OIB
E-MORB
N-MORB
n30
n50
n8
n2
(b)
Cooperdock et al., 2018
AOC
Miller et al., 2009
New cal
Catalina mélange
Harz
GLOSS
CaO (Ox%)
MgO (Ox%)
1
2
3
4
5
(c)
p165
p125
p1
581
p30
p5
p135
n290
n57
n1
n2
n10
n30
n50
n8
Cr_N
Eu_N/Eu_N*
L
G
n290
n57
n10
n1
p5
p125
p135
p165
n50
n30
n8
n2
p1
p30
581
(d)
Cr (µg/g)
Al2O3 (wt. %)
(e)
TiO2 (wt. %)
(f)
Zr (µg/g)
(g) Transect L
Cooperdock et al. 2018
MORB
Whole rock/chondrite
n290
n57
n10
n1
p5
p125
p135
p165
(h) Transect G and 581
Cooperdock et al. 2018
MORB
n50
n30
n8
n2
p1
p30
581
B Rb Th Sr Ta Hf Sc As Ce Nd Eu Tb Ho Tm Lu Ni
Li Cs Ba Pb Nb Zr Y V La Pr Sm Gd Dy Er Yb Co Cr

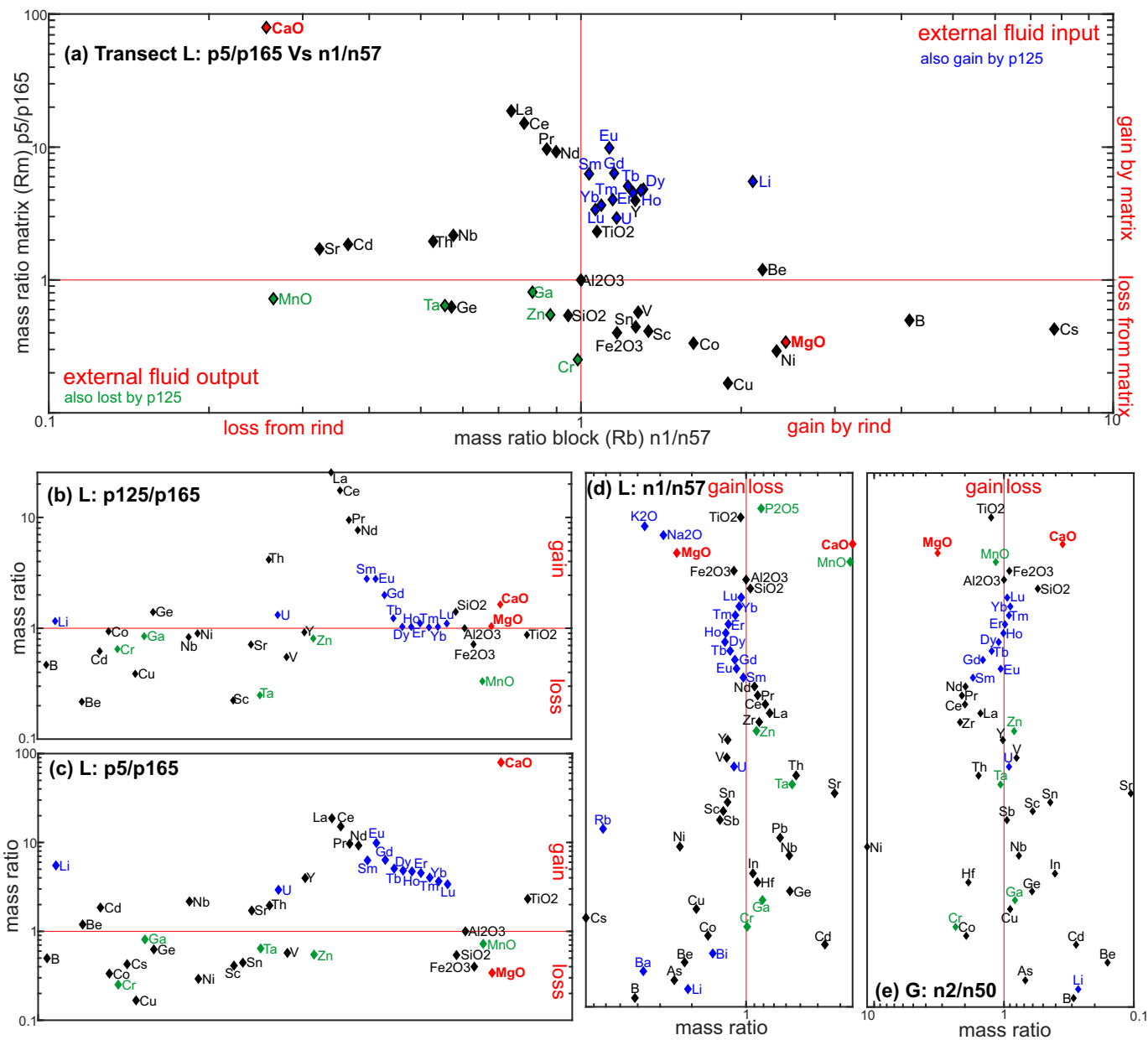
(a) Transect L: p5/p165 Vs n1/n57
external fluid input
also gain by p125
external fluid output
also lost by p125
loss from rind
gain by rind
loss from matrix
gain by matrix
mass ratio matrix (Rm) p5/p165
mass ratio block (Rb) n1/n57
(b) L: p125/p165
(c) L: p5/p165
(d) L: n1/n57 gain loss
(e) G: n2/n50
gain
loss
mass ratio

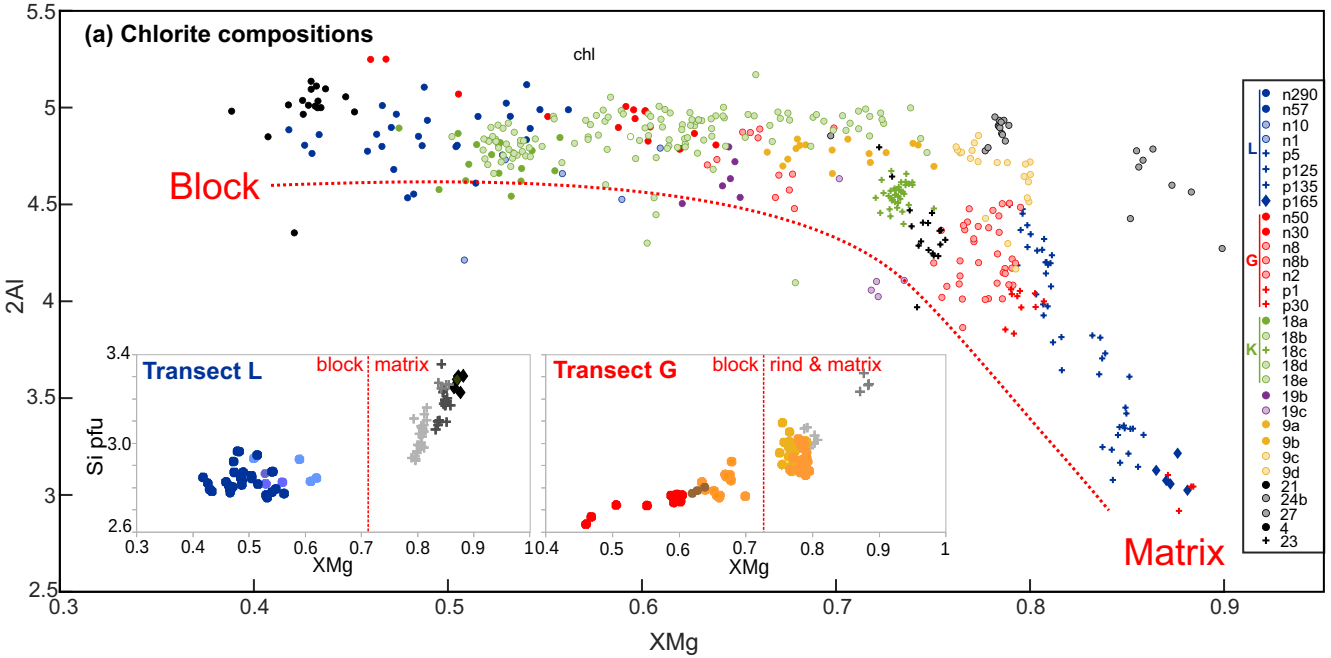
(a) Chlorite compositions
chl
Block
Matrix
2Al
XMg
Transect L
block
matrix
Transect G
block
rind & matrix
Si pfu
XMg
L
n290
n57
n10
n1
p5
p125
p135
p165
G
n50
n30
n8
n8b
n2
p1
p30
K
18a
18b
18c
18d
18e
19b
19c
9a
9b
9c
9d
21
24b
27
4
23

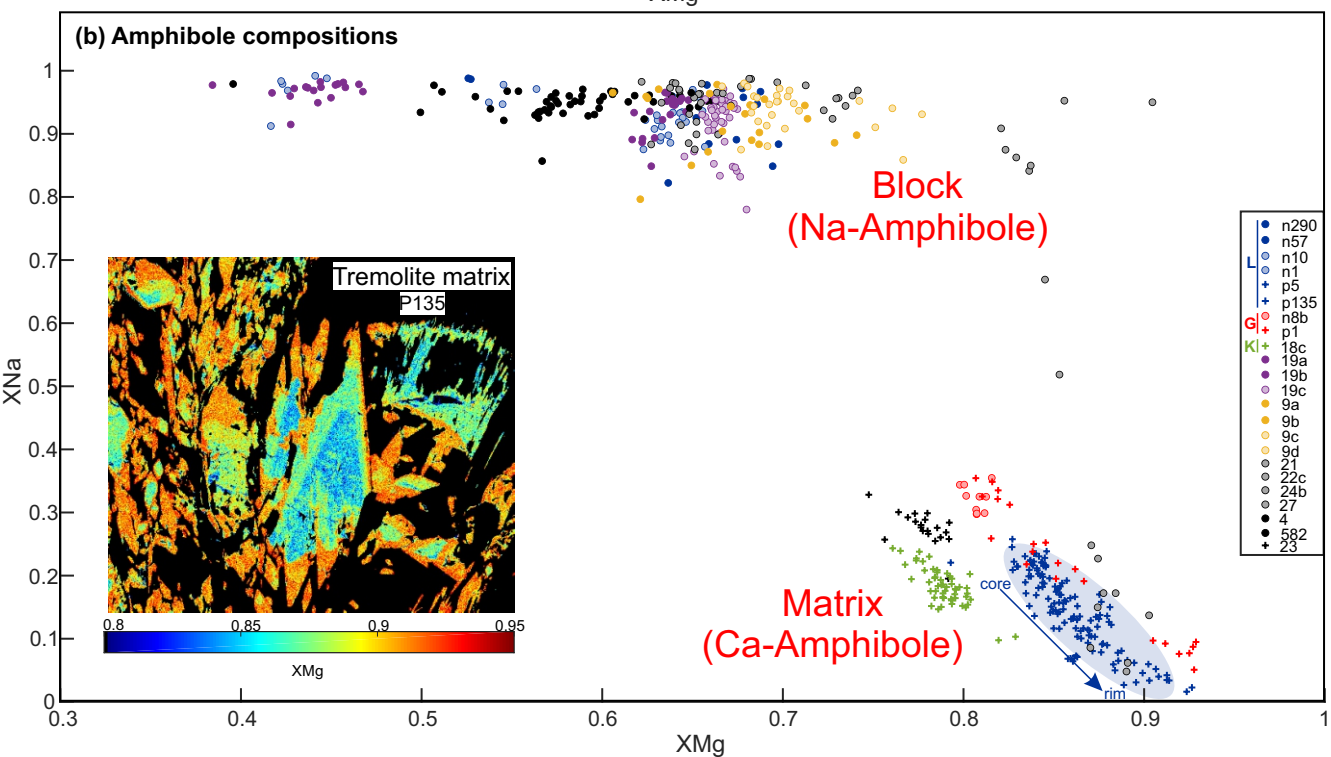
(b) Amphibole compositions
Block
(Na-Amphibole)
Tremolite matrix
P135
XMg
Matrix
(Ca-Amphibole)
core
rim
XNa
XMg
L
n290
n57
n10
n1
p5
p135
G
n8b
p1
K
18c
19a
19b
19c
9a
9b
9c
9d
21
22c
24b
27
4
582
23

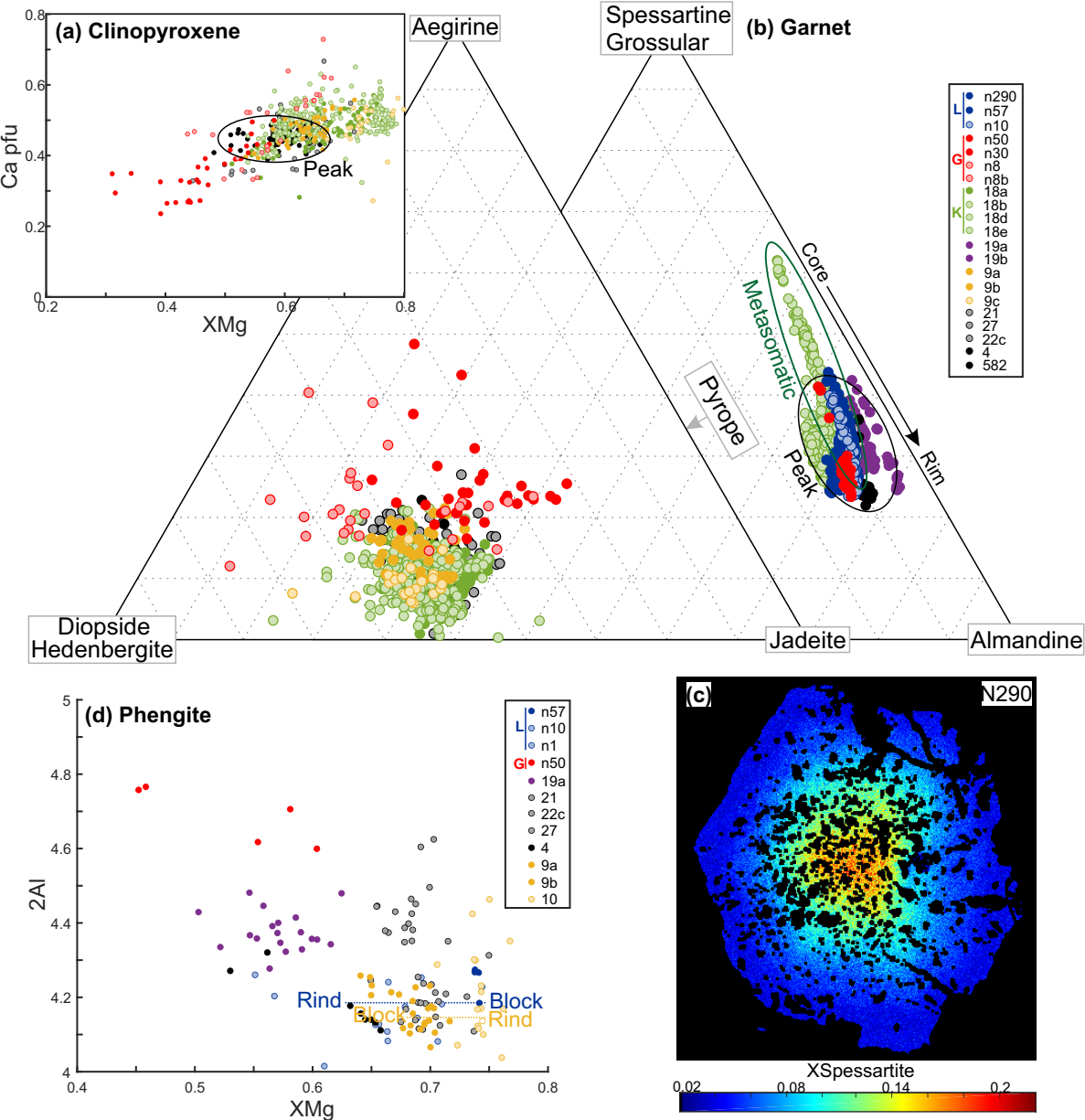
(a) Clinopyroxene
Ca pfu
XMg
Peak
Aegirine
Diopside
Hedenbergite
Jadeite
(b) Garnet
Spessartine
Grossular
Almandine
Core
Rim
Metasomatic
Peak
Pyrope
L
n290
n57
n10
G
n50
n30
n8
n8b
K
18a
18b
18d
18e
19a
19b
9a
9b
9c
21
27
22c
4
582
(d) Phengite
2Al
XMg
n57
n10
n1
n50
19a
21
22c
27
4
9a
9b
10
Rind
Block
Block
Rind
(c)
N290
XSpessartite
0.02
0.08
0.14
0.2

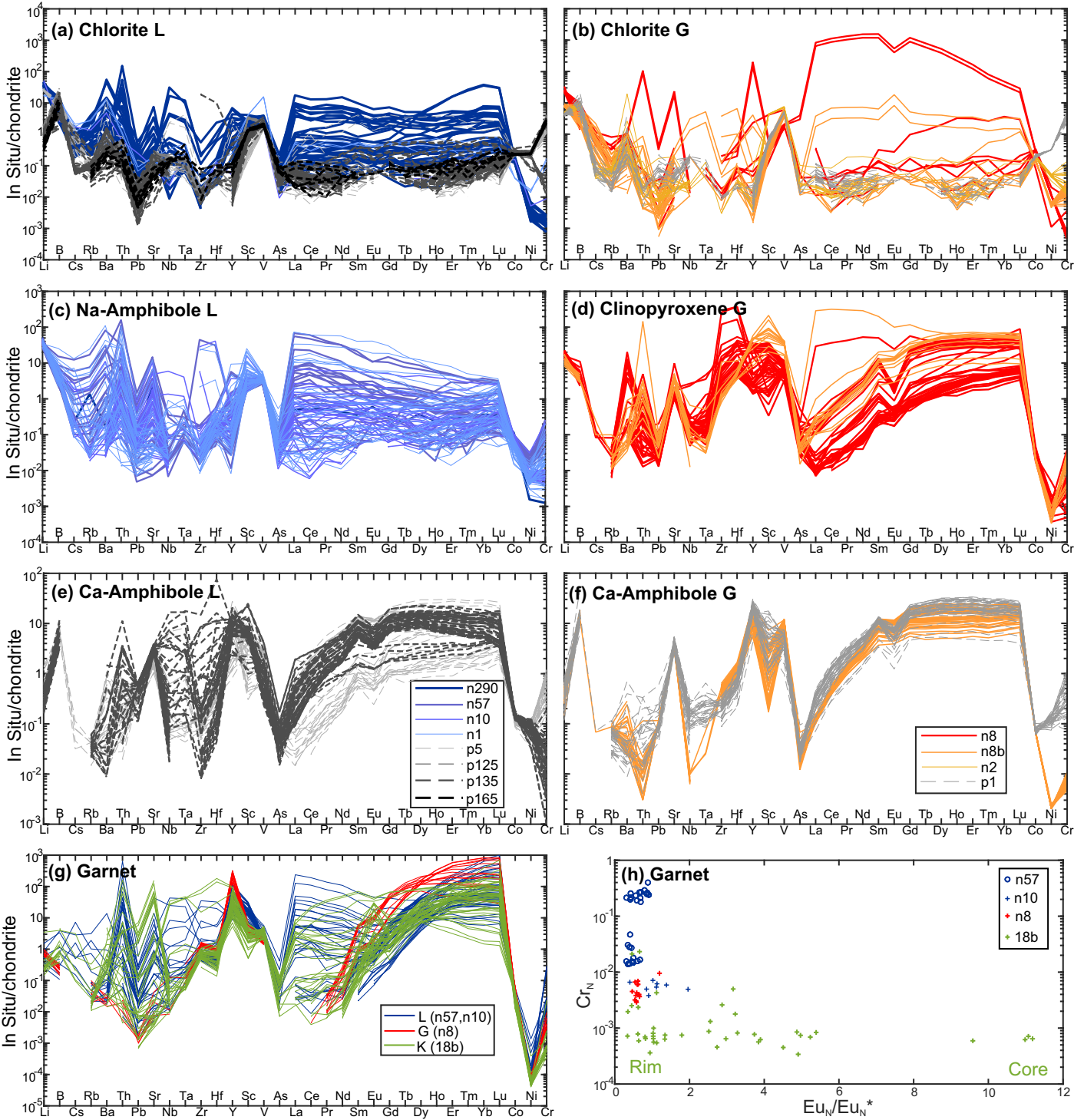
(a) Chlorite L
(b) Chlorite G
(c) Na-Amphibole L
(d) Clinopyroxene G
(e) Ca-Amphibole L
(f) Ca-Amphibole G
(g) Garnet
(h) Garnet
In Situ/chondrite
B Rb Th Sr Ta Hf Sc As Ce Nd Eu Tb Ho Tm Lu Ni
Li Cs Ba Pb Nb Zr Y V La Pr Sm Gd Dy Er Yb Co Cr
n290
n57
n10
n1
p5
p125
p135
p165
n8
n8b
n2
p1
L (n57,n10)
G (n8)
K (18b)
n57
n10
n8
18b
Rim
Core
Cr_N
Eu_N/Eu_N^*

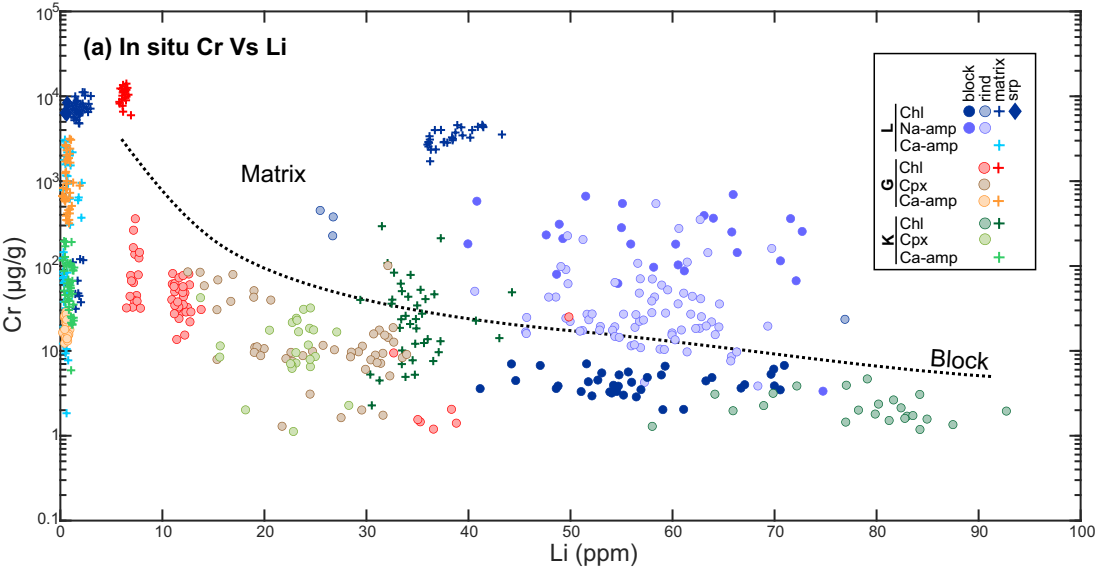
(a) In situ Cr Vs Li
Matrix
Block
Cr (µg/g)
Li (ppm)
block
rind
matrix
srp
L
Chl
Na-amp
Ca-amp
G
Chl
Cpx
Ca-amp
K
Chl
Cpx
Ca-amp

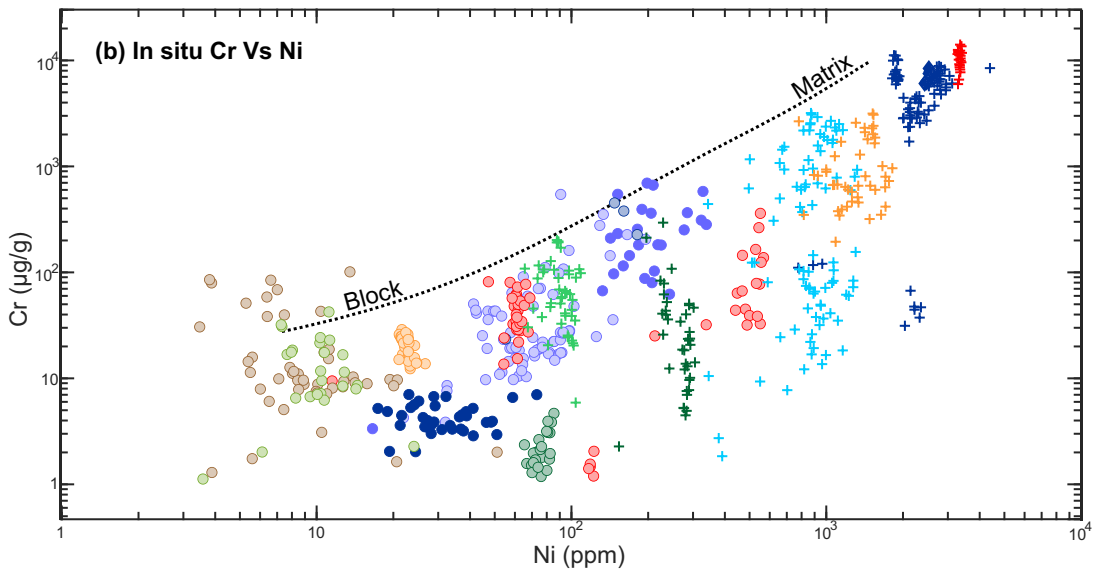
(b) In situ Cr Vs Ni
Matrix
Block
Cr (µg/g)
Ni (ppm)

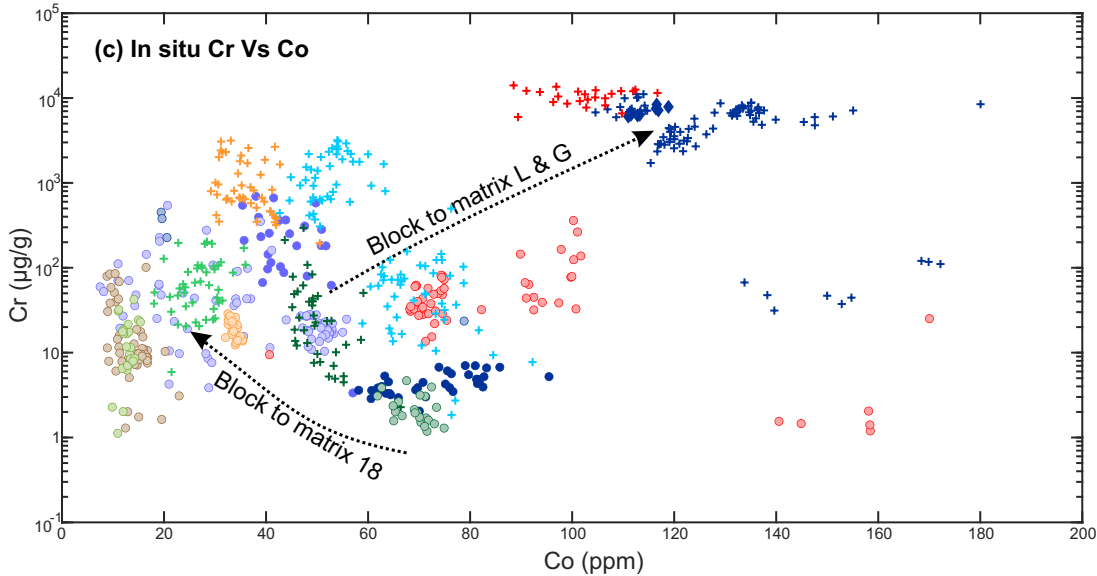
(c) In situ Cr Vs Co
Block to matrix L & G
Block to matrix 18
Cr (µg/g)
Co (ppm)

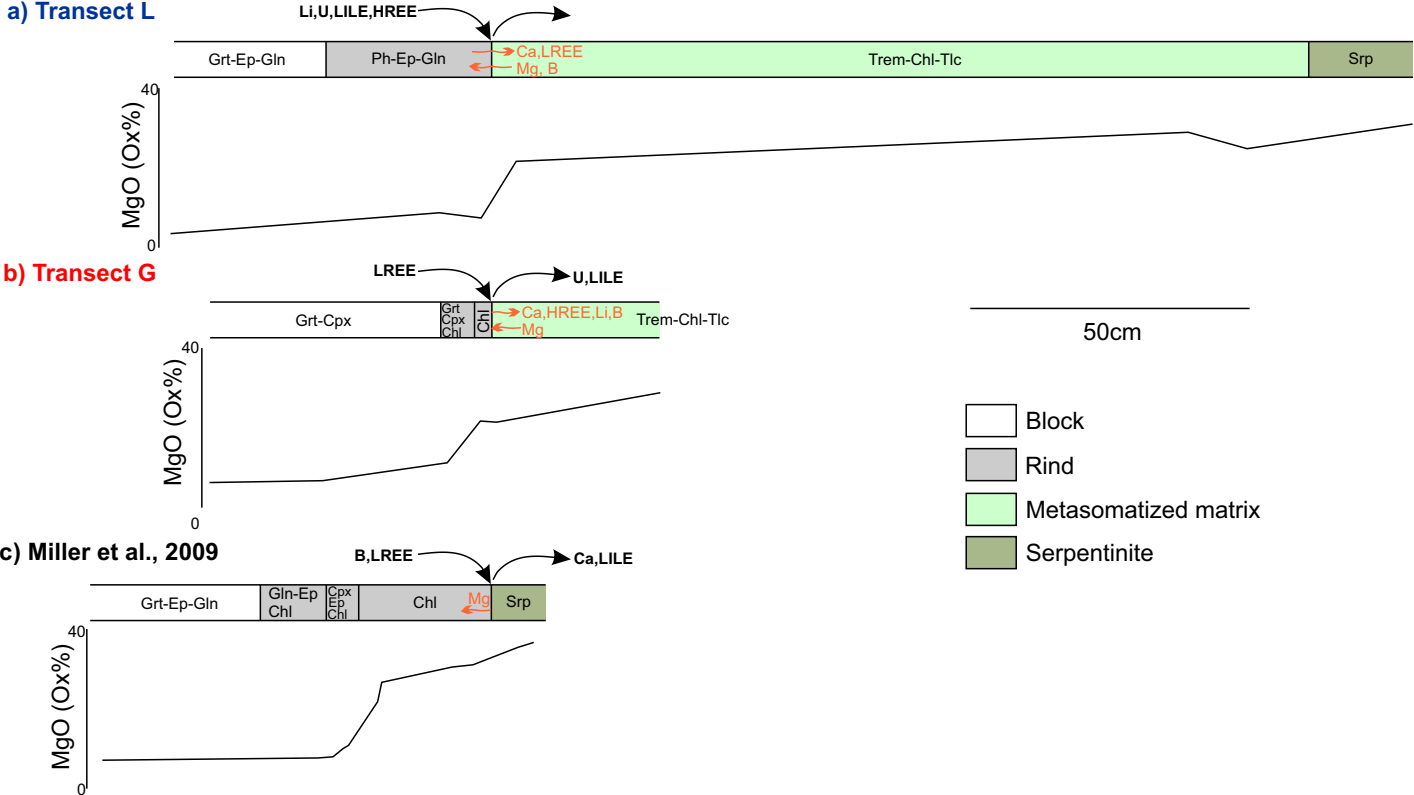
a) Transect L
Li,U,LILE,HREE
Grt-Ep-Gln
Ph-Ep-Gln
Ca,LREE
Mg, B
Trem-Chl-Tlc
Srp
MgO (Ox%)
40
0
b) Transect G
LREE
U,LILE
Grt-Cpx
Grt
Cpx
Chl
Chl
Ca,HREE,Li,B
Mg
Trem-Chl-Tlc
MgO (Ox%)
40
0
50cm
Block
Rind
Metasomatized matrix
Serpentinite
c) Miller et al., 2009
B,LREE
Ca,LILE
Grt-Ep-Gln
Gln-Ep
Chl
Cpx
Ep
Chl
Chl
Mg
Srp
MgO (Ox%)
40
0

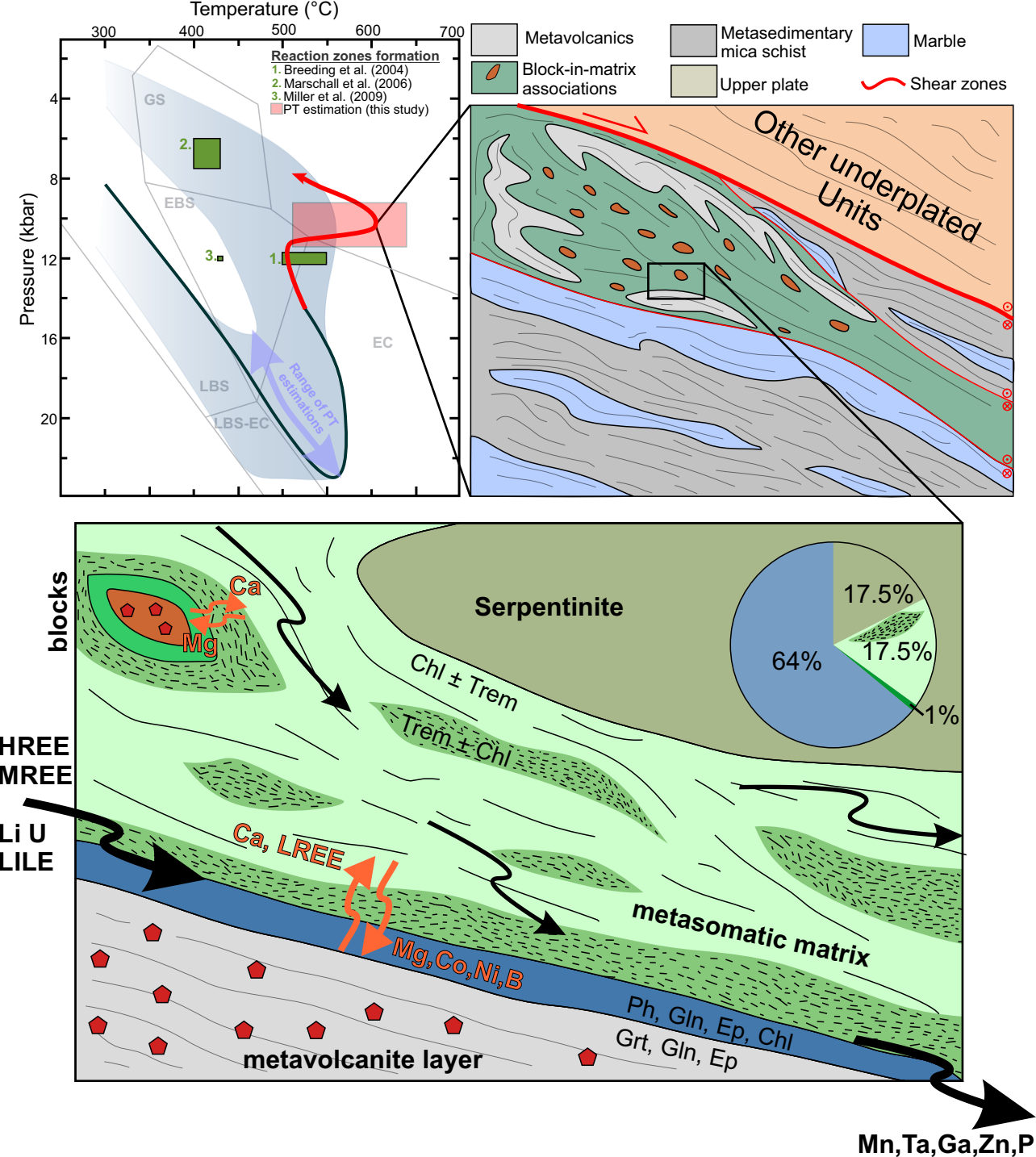
Temperature (°C)
300
400
500
600
700
Pressure (kbar)
4
8
12
16
20
Reaction zones formation
1. Breeding et al. (2004)
2. Marschall et al. (2006)
3. Miller et al. (2009)
PT estimation (this study)
GS
EBS
EC
LBS
LBS-EC
Range of PT estimations
Metavolcanics
Block-in-matrix associations
Metasedimentary mica schist
Upper plate
Marble
Shear zones
Other underplated Units
blocks
Ca
Mg
Serpentinite
17.5%
17.5%
64%
1%
Chl ± Trem
Trem ± Chl
HREE
MREE
Li U
LILE
Ca, LREE
Mg,Co,Ni,B
metasomatic matrix
Ph, Gln, Ep, Chl
Grt, Gln, Ep
metavolcanite layer
Mn,Ta,Ga,Zn,P

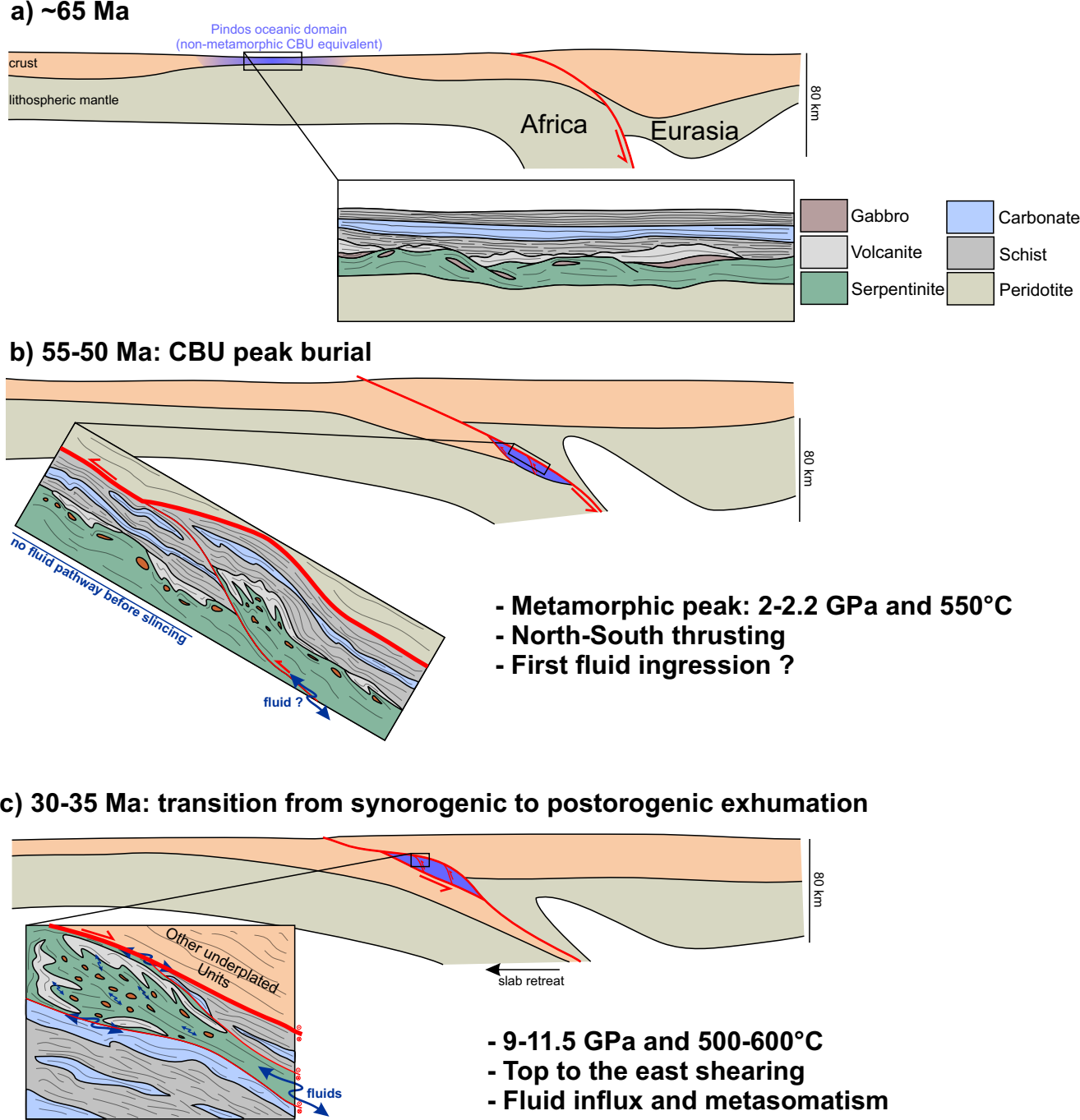
a) ~65 Ma
Pindos oceanic domain
(non-metamorphic CBU equivalent)
crust
lithospheric mantle
Africa
Eurasia
80 km
Gabbro
Volcanite
Serpentinite
Carbonate
Schist
Peridotite
b) 55-50 Ma: CBU peak burial
80 km
no fluid pathway before slincing
fluid ?
- Metamorphic peak: 2-2.2 GPa and 550°C
- North-South thrusting
- First fluid ingression ?
c) 30-35 Ma: transition from synorogenic to postorogenic exhumation
80 km
Other underplated
Units
slab retreat
fluids
- 9-11.5 GPa and 500-600°C
- Top to the east shearing
- Fluid influx and metasomatism